

From cosmological simulations to binary black hole mergers:

The impact of using analytical star formation history models on gravitational-wave source populations

SASHA LEVINA ^{1,2} FLOOR BROEKGAARDEN ,¹ LIEKE VAN SON ,³ EMANUELE BERTI ,² AMEDEO ROMAGNOLO ,^{1,4,5,6}
RUEDIGER PAKMOR ,⁷ AND ANA LAM ,⁸¹Department of Astronomy & Astrophysics, University of California, San Diego, 9500 Gilman Drive, La Jolla, CA 92093, USA²William H. Miller III Department of Physics and Astronomy, Johns Hopkins University, 3400 N. Charles Street, Baltimore, Maryland, 21218, USA³Radboud University, Faculty of Science, Huygensgebouw, Heyendaalseweg 135, 6525 AJ Nijmegen, The Netherlands⁴Nicolaus Copernicus Astronomical Center, Polish Academy of Sciences, ul. Bartycka 18, 00-716 Warsaw, Poland⁵Universität Heidelberg, Zentrum für Astronomie (ZAH), Institut für Theoretische Astrophysik, Albert Ueberle Str. 2, 69120, Heidelberg, Germany⁶Dipartimento di Fisica e Astronomia Galileo Galilei, Università di Padova, Vicolo dell'Osservatorio 3, I-35122 Padova, Italy⁷Max Planck Institute for Astrophysics, Karl-Schwarzschild-Str. 1, D-85748 Garching, Germany⁸Department of Astronomy, Columbia University, 538 West 120th Street, New York, NY 10027, USA

ABSTRACT

Observations of binary black hole (BBH) mergers provide a unique window into the lives of massive stars across cosmic time. Connecting redshift-dependent merger properties to massive star progenitors requires accurate models of cosmic star formation and chemical enrichment histories. Analytical fits for the metallicity-specific cosmic star formation rate density $\mathcal{S}(Z, z)$ are commonly used as proxies for the complex underlying star formation history, yet they remain unconstrained. Using the IllustrisTNG cosmological simulations, we evaluate the accuracy of these analytical $\mathcal{S}(Z, z)$ prescriptions and assess how simulation resolution and volume affect the inferred $\mathcal{S}(Z, z)$. By coupling the simulated and analytical $\mathcal{S}(Z, z)$ to the population synthesis code COMPAS, we investigate the resulting BBH merger rates and mass distributions. We find that analytical $\mathcal{S}(Z, z)$ prescriptions can overestimate BBH merger rates at high redshift ($z \gtrsim 6$) by up to a factor of $10\text{--}10^4$, depending on cosmological simulation resolution, and can introduce spurious features in the BBH mass distribution. For example, they can produce an artificial feature near $8 M_\odot$ in the primary mass distribution at $z \lesssim 2$, which is absent when using the full simulation-based $\mathcal{S}(Z, z)$, while simultaneously suppressing high-mass features. These discrepancies arise because simple analytical models fail to capture a high-metallicity bump and a more flattened low-metallicity tail in the simulated $\mathcal{S}(Z, z)$ metallicity distribution. Our results highlight the importance of accurate star formation histories for modeling BBH populations, demonstrate the limitation of widely used analytical $\mathcal{S}(Z, z)$ fits, and underscore the need for careful integration of cosmological simulations, analytical fits, and population synthesis when interpreting gravitational-wave observations.

1. INTRODUCTION

The mergers of BBHs, even those occurring nearby, encode information about stellar physics across a large range of redshifts due to the distribution of delay times between their formation and merger (M. Fishbach & V. Kalogera 2021; I. Mandel & A. Farmer 2022; M. Fishbach & L. van Son 2023; M. Chrušlińska 2024). To disentangle the mixture of delay times and formation channels within an observed gravitational wave (GW) population and to infer the environments and binary evo-

lutionary processes that produce merging BBHs, astrophysical population synthesis models of their formation pathways are essential (F. S. Broekgaarden et al. 2021, 2022; I. Mandel & F. S. Broekgaarden 2022). These models must be combined with assumptions about the cosmic star formation history in order to accurately represent stellar progenitors across cosmic epochs (e.g., C. J. Neijssel et al. 2019; M. Chrušlińska et al. 2019; F. S. Broekgaarden et al. 2022; A. P. Boesky et al. 2024).

In modeling rates of metallicity-dependent transients (e.g., BBH mergers), the star formation history is commonly represented using a simple, fitted functional form that combines a star formation rate density $\mathcal{S}(z)$ with some assumption for the metallicity distribution across

Corresponding author: Sasha Levina
Email: slevina@ucsd.edu

redshift (e.g., C. J. Neijssel et al. 2019). The resulting metallicity-dependent star formation rate density $\mathcal{S}(Z, z)$ can vary significantly depending on the model, how it is constructed, and the data used to calibrate its parameters (see M. Chruścińska 2024; M. Chruścińska et al. 2025). Rates of double compact object mergers across redshift may change by an order of magnitude depending on the assumptions made for $\mathcal{S}(Z, z)$ (M. Chruścińska et al. 2019; C. J. Neijssel et al. 2019; F. Santoliquido et al. 2021; F. S. Broekgaarden et al. 2022; L. A. C. van Son et al. 2023). Testing the effect of different models of $\mathcal{S}(Z, z)$ can help disentangle the effects of metallicity evolution, the star formation rate (SFR), and binary evolution models on the BBH population and provide insight into which components are most critical to model accurately.

Three methods are typically used to model the star formation history: (i) analytical prescriptions, (ii) observational distributions, or (iii) cosmological simulations. Analytical prescriptions for $\mathcal{S}(z)$ and the redshift-dependent metallicity distribution (as employed by e.g., N. Langer & C. A. Norman 2006; P. Madau & M. Dickinson 2014; P. Madau & T. Fragos 2017; C. J. Neijssel et al. 2019; P. N. Tang et al. 2020; F. Santoliquido et al. 2020; A. P. Boesky et al. 2024; T. Smith & M. Kaplinghat 2024; C. Sgalletta et al. 2024; K. Turbang et al. 2024; A. Schiebelbein-Zwack & M. Fishbach 2024) are derived from galaxy survey data or empirical scaling relations such as $\mathcal{S}(z)$, the mass-metallicity relation (MZR), and the galaxy mass function, the number density of galaxies per logarithmic mass bin (GSMF). Observational data can also be directly used to create a distribution of star formation histories without performing an analytical fit (M. Chruścińska et al. 2019; M. Chruścińska & G. Nelemans 2019; L. Boco et al. 2021; C. Sgalletta et al. 2024). However, observations become increasingly challenging at high redshifts and low galaxy luminosities, with uncertainties in high-redshift dust extinction, survey sensitivity and sky coverage limits, and discrepancies between star formation histories derived from different observational methods (M. Chruścińska & G. Nelemans 2019; A. Katsianis et al. 2020, 2021; A. Enia et al. 2022; B. Magnelli et al. 2024). This makes it more challenging to construct a comprehensive cosmic star formation history.

Cosmological simulations offer a third approach by modeling a representative population of galaxies across cosmic history. These simulations track the characteristics of stellar populations and the gas from which they form over redshift (for a review, see M. Vogelsberger et al. 2020). This enables the construction of the complete $\mathcal{S}(Z, z)$ from the SFR and metallicity of galaxies,

accounting for every galaxy formed in the simulation box without observational limitations (e.g., H. S. Hwang et al. 2019; M. M. Briel et al. 2022). The accuracy of that star formation history is constrained by the model resolution, physical assumptions built into the simulation, and the treatment of unresolved processes via subgrid models (A. Pillepich et al. 2018a; M. Vogelsberger et al. 2020; R. Pakmor et al. 2022). Different simulations can deviate particularly at high redshifts, as high redshift galaxy evolution is not directly accounted for in the model calibration. The resulting BBH merger rate can vary significantly with simulation used (M. M. Briel et al. 2022). Others use the cosmological simulation $\mathcal{S}(Z, z)$ implicitly by populating BBHs (or other transients) into the simulation by associating them with stellar populations in the simulation (e.g., M. Mapelli et al. 2017; M. Mapelli & N. Giacobbo 2018; M. Mapelli et al. 2019; M. C. Artale et al. 2019, 2020; F. Marinacci et al. 2025). More recently, analytical fits to cosmological simulations have been used to represent $\mathcal{S}(Z, z)$ (L. A. C. van Son et al. 2023), which is computationally simpler for further use with population synthesis than constructing $\mathcal{S}(Z, z)$ from the simulation data. These fits have become widely used (e.g. L. A. C. van Son et al. 2022a; D. D. Hendriks et al. 2023; J. Riley & I. Mandel 2023; S. K. Roy et al. 2025; R. Willcox et al. 2025).

The main challenge in modeling BBH populations using analytical fits to cosmological simulations is twofold. First, it is unclear whether analytical prescriptions can reliably represent the underlying $\mathcal{S}(Z, z)$. Second, the impact of simulation resolution and box size on the star formation history, and hence on the predicted BBH population, remains insufficiently understood. Several studies have addressed parts of this problem. L. A. C. van Son et al. (2023) tested the goodness of fit of analytical $\mathcal{S}(Z, z)$ models to a single IllustrisTNG simulation and examined how varying $\mathcal{S}(Z, z)$ parameters affects the BBH primary mass distribution. M. M. Briel et al. (2022) explored how different cosmological simulation suites influence predicted BBH population properties. C. Sgalletta et al. (2024) compared analytical $\mathcal{S}(Z, z)$ prescriptions with observationally derived models when computing the BBH merger rate. With respect to numerical effects, F. Marinacci et al. (2025) found that variations in box size have a negligible effect on $\mathcal{S}(Z, z)$ and on the resulting BBH properties. By contrast, resolution effects are known to systematically affect $\mathcal{S}(Z, z)$. Higher-resolution simulations tend to yield higher star formation rate normalizations (A. Pillepich et al. 2018a). Some simulation suites mitigate this by recalibrating their subgrid models at each resolution (see F. Marinacci

et al. 2014). However, the consequences of resolution variations for modeling BBH populations have not yet been studied in a systematic way. A quantitative assessment of both analytical modeling choices and numerical effects is therefore essential. An accurate description of the cosmic star formation history is a prerequisite for robust predictions of the BBH merger population. This motivates the analysis we present in this work.

In this paper, we quantify the impacts of approximating the star formation history of cosmological simulations using analytical models and investigate the effect of cosmological simulation resolution on the BBH merger population. We fit analytical $\mathcal{S}(Z, z)$ models to three cosmological simulations of varying resolution and box size in the IllustrisTNG suite, and compare the resulting star formation histories and BBH population properties using the binary population synthesis code **COMPAS** (Compact Object Mergers: Population Astrophysics and Statistics, J. Riley et al. 2022).

2. METHODS

The metallicity-dependent star formation rate density $\mathcal{S}(Z, z)$ quantifies the amount of stellar mass formed per unit comoving volume, redshift, and metallicity. In this study, we construct $\mathcal{S}(Z, z)$ in two ways: (i) directly based on the IllustrisTNG simulations (see Section 2.1), and (ii) using an analytical fit that is often used in the field to represent $\mathcal{S}(Z, z)$ for the TNG simulation (see Section 2.2). We use both in the convolution (cosmic integration, see Section 2.3) to model the BBH merger population and investigate how using an analytical fit causes deviations from directly using the underlying distribution from the TNG simulations with different resolutions (see Section 2.4).

2.1. Obtaining the TNG simulation $\mathcal{S}(Z, z)$

We derive the simulation-based $\mathcal{S}(Z, z)$ from the IllustrisTNG simulations (D. Nelson et al. 2019a; A. Pillepich et al. 2018b; F. Marinacci et al. 2018; J. P. Naiman et al. 2018; D. Nelson et al. 2018, 2019b; A. Pillepich et al. 2019). IllustrisTNG is a suite of magnetohydrodynamical cosmological simulations performed with the moving-mesh code AREPO (V. Springel 2010) and adopting cosmological parameters $\Omega_M = 0.3089$, $\Omega_\Lambda = 0.691$, $\sigma_8 = 0.8159$, $n_s = 0.9667$, $h = 0.6774$, $H_0 = 67.8$ (Planck Collaboration 2016).

The IllustrisTNG simulations span three primary volumes: TNG50-1, TNG100-1, and TNG300-1, with comoving box volumes with side lengths of approximately 50, 100, and 300 Mpc and baryonic mass resolutions of 5.7×10^4 , 9.4×10^5 , and $7.6 \times 10^6 M_\odot/h$, respectively. The highest resolution box, TNG50-1, resolves

the internal structure of galaxies, including stellar populations and gas inflows and outflows. On the other hand, TNG300-1, while lower in resolution, captures a representative population of galaxy clusters and provides advantages through providing a larger statistical sample, but does not form low-mass galaxies below its minimum resolution. TNG100-1 offers an intermediate balance between resolution and volume, it is directly comparable to the predecessor Illustris simulations (D. Nelson et al. 2019a), and it is more similar to other cosmological simulations. In the following, we focus on the highest-resolution realizations of each box (TNG50-1, TNG100-1, and TNG300-1).

Each TNG simulation consists of data output at 100 redshift snapshots from $z = 20$ to $z \approx 0$. Snapshots include the full set of resolution elements (gas, dark matter, stars, etc.) for each cells in the box at that redshift snapshot, divided into smaller “chunks” for data handling. For our analysis we only use the gas cells (“PartType0”), as they contain the metallicity and instantaneous SFR information needed to compute $\mathcal{S}(Z, z)$.

Star formation occurs in cells with gas densities exceeding $n_H \gtrsim 0.1 \text{ cm}^{-3}$, following the Kennicutt-Schmidt relation prescription (M. Schmidt 1959; R. C. Kennicutt 1989). Star formation occurs stochastically and typically converts a cell fully into a single star particle. If that happens, the star particle represents an unresolved stellar population with the mass of the star forming cell, which is within a factor of two of the target baryonic mass resolution of the simulation (R. Pakmor et al. 2022). The metallicity of a gas cell, defined as the mass fraction of all elements heavier than helium, characterizes the metallicity of the associated stellar population.

To construct the simulation $\mathcal{S}(Z, z)$, we bin all star-forming gas cells in each snapshot by metallicity. We use 60 logarithmically-spaced metallicity bins between the minimum TNG metallicity of $\log_{10} Z = -10$ and the maximum $\log_{10} Z = 0$, summing the SFR of all gas cells in each bin. Note that the choice of binning here does not affect the final results. The resulting $\mathcal{S}(Z, z)$ is normalized by the comoving simulation volume to yield units of $M_\odot \text{ yr}^{-1} \text{ Mpc}^{-3}$. We also retrieve the overall gas metallicity distribution through binning per snapshot, $dP/d \log Z$, and record this for later comparison.

To ensure smooth coverage across metallicity and redshift, we do a linear interpolation on the simulation $\mathcal{S}(Z, z)$ over the range $0 < z < 14$ with steps of $\Delta z = 0.05$ and 500 logarithmic metallicity bins. The interpolation is performed in lookback time (rather than redshift) using the Planck Collaboration (2016) cosmology, consistent with that adopted in IllustrisTNG.

2.2. Modeling the metallicity-dependent star formation rate density with an analytical fit

The metallicity-dependent star formation rate density $\mathcal{S}(Z, z)$ is often modeled as the product of the total star formation rate density and a metallicity distribution (e.g., M. Dominik et al. 2013; M. Chruścińska et al. 2019; M. Chruścińska & G. Nelemans 2019; C. J. Neijssel et al. 2019; F. S. Broekgaarden et al. 2021; L. A. C. van Son et al. 2023). This product is represented by using an analytical fit because it is simple, fast, convenient for uncertainty quantification, and parametrizes the distribution into physical variables (C. J. Neijssel et al. 2019; L. A. C. van Son et al. 2023; R. Willcox et al. 2025). We investigate whether such analytical fits are a reliable approximation for $\mathcal{S}(Z, z)$ by fitting the L. A. C. van Son et al. (2023) $\mathcal{S}(Z, z)$ prescription to the TNG simulations. The analytical $\mathcal{S}(Z, z)$ is constructed by combining the total star formation rate density, $\mathcal{S}(z)$, with a skewed log-normal metallicity distribution, $dP/dZ(Z, z)$:

$$\mathcal{S}(Z, z) = \mathcal{S}(z) \times \frac{dP}{dZ}(Z, z). \quad (1)$$

The quantity $\mathcal{S}(z)$ is the total mass formed, per comoving volume per year. It is defined using the functional form of P. Madau & M. Dickinson (2014):

$$\mathcal{S}(z) = a \frac{(1+z)^b}{1 + [(1+z)/c]^d}, \quad (2)$$

where a is a normalization factor, b characterizes the low redshift slope (where $\mathcal{S}(z)$ scales as $(1+z)^b$ away from the peak at low z), c defines the location of the peak, and d dominates the high redshift slope (see Appendix A.1 of F. Iacobelli et al. 2022). The P. Madau & T. Fragos (2017) values for $\mathcal{S}(z)$ parameters are $a = 0.01$, $b = 2.6$, $c = 3.2$, and $d = 6.2$.

For the metallicity distribution function $dP/dZ(Z, z)$, we adopt a skewed log-normal distribution in metallicity and redshift following L. A. C. van Son et al. (2023), defined as

$$\frac{dP}{dZ}(Z, z) = \frac{2}{\omega(z)Z} \times \phi \left(\frac{\ln Z - \xi(z)}{\omega(z)} \right) \Phi \left(\alpha \frac{\ln Z - \xi(z)}{\omega(z)} \right), \quad (3)$$

where ϕ is the standard log-normal distribution,

$$\phi \left(\frac{\ln Z - \xi}{\omega} \right) = \frac{1}{\sqrt{2\pi}} \exp \left[-\frac{1}{2} \left(\frac{\ln Z - \xi}{\omega} \right)^2 \right]; \quad (4)$$

and Φ is its cumulative distribution function,

$$\Phi \left(\alpha \frac{\ln Z - \xi}{\omega} \right) = \frac{1}{2} \left[1 + \text{erf} \left(\alpha \frac{\ln Z - \xi}{\omega\sqrt{2}} \right) \right]. \quad (5)$$

The “skewness” parameter α introduces asymmetry into the distribution. The function $\xi(z)$ determines the median of the distribution and is given by

$$\xi(z) = \ln \left[\frac{\mu_0 10^{\mu_z z}}{2\Phi(\alpha\omega/\sqrt{1+\alpha^2})} \right] - \frac{\omega^2}{2}. \quad (6)$$

The metallicity distribution function $dP/dZ(Z, z)$ is characterized by five physically motivated parameters: μ_0 , μ_z , ω_0 , ω_z , and α . The parameter μ_0 sets the mean metallicity at $z \approx 0$, while μ_z describes its redshift evolution according to $\mu(z) = \mu_0 10^{\mu_z z}$ (e.g. N. Langer & C. A. Norman 2006; C. J. Neijssel et al. 2019; L. A. C. van Son et al. 2023). The width of the metallicity distribution is represented by ω_0 at $z \approx 0$ and evolves across redshift as $\omega(z) = \omega_0 10^{\omega_z z}$. The final parameter, α , encodes the asymmetry of the metallicity distribution: $\alpha = 0$ corresponds to a symmetric log-normal distribution, while $\alpha < 0$ produces a longer low-metallicity tail. Following L. A. C. van Son et al. (2023), we assume that α does not evolve with redshift; see L. A. C. van Son et al. (2023) for a more detailed discussion of this parameterization. Together, the parameters describing $\mathcal{S}(z)$ and $dP/dZ(Z, z)$ define a nine-parameter analytical fit that is often used to represent $\mathcal{S}(Z, z)$. We will be using this $\mathcal{S}(Z, z)$ for the analytical fit to the TNG simulations.

Finally, we fit the analytical model described above to the interpolated simulation $\mathcal{S}(Z, z)$ described in Section 2.1 using the optimization framework of L. A. C. van Son et al. (2023) to obtain the best-fit analytical $\mathcal{S}(Z, z)$ to each TNG. We employ the SciPy v1.8.1 implementations of the BFGS optimization algorithm (J. Nocedal & S. Wright 2006) for TNG50-1 and TNG100-1, and the Nelder–Mead method (F. Gao & L. Han 2012) for TNG300-1, as the latter shows improved convergence for lower-resolution data.

2.3. Calculating BBH merger rates and properties over redshift with COMPAS

COMPAS (J. Riley et al. 2022) is a rapid binary population synthesis code that is based on the stellar and binary evolution prescriptions of J. R. Hurley et al. (2000, 2002). We use COMPAS version v02.26.03 and adopt the simulations from L. A. C. van Son et al. (2022b,a), publicly available at L. van Son (2023). The simulations contain 10^7 binaries, selected using the adaptive importance sampling for binary black hole mergers STROOP-WAFEL (F. S. Broekgaarden et al. 2019). Primary masses (M_1) were drawn from the P. Kroupa (2001) initial mass function over the range $10 \leq M_1/M_\odot \leq 150$. Secondary masses (M_2) were selected from a uniform mass ratio distribution, $q = M_2/M_1$, with $0.01 \leq q \leq$

1.0 and $M_2 \geq 0.1 M_\odot$. Birth metallicities were drawn from a flat distribution in log-space between $10^{-4} \leq Z \leq 0.03$. The initial orbital separation follows a flat-in-log distribution in the range from 0.01 to 1000 AU. All binaries are assumed to be born circular at birth, consistent with observations that OB stars (likely progenitors of BBHs) tend to have circular orbits (I. Vargas-Salazar et al. 2025). Mass transfer events would further circularize the binary (as is implemented in **COMPAS** following, e.g., J. R. Hurley et al. 2002; K. Belczynski et al. 2002, 2008). It is important to note that it has been recently shown that a substantial fraction of binaries may retain eccentricity following an eccentric mass transfer event (K. A. Rocha et al. 2025). For additional details on the **COMPAS** simulation, see L. A. C. van Son et al. (2022b).

2.4. Comparing the analytical fit and simulation $\mathcal{S}(Z, z)$ method

To study the impact of using the analytical fit for $\mathcal{S}(Z, z)$, we compare the analytical fit and simulation $\mathcal{S}(Z, z)$ through two different methods. First, we compare $\mathcal{S}(Z, z)$ that the two methods produce. Second, we also investigate the BBH properties (rates and mass distributions across redshift) that each method results in and compare this to observations.

For comparing the BBH properties, we convert the synthetic binary population from **COMPAS** into a cosmic merger rate density for BBH binaries by combining the binary formation efficiencies and BBH properties from **COMPAS** with either the analytical fit or the TNG simulation $\mathcal{S}(Z, z)$ model using the **COMPAS** code. The calculation of BBH merger rates and properties across redshift using “cosmic integration” post-processing scripts is based on the framework developed by C. J. Neijssel et al. (2019), enabling flexible modeling of $\mathcal{S}(Z, z)$ through the parametrized model described in Section 2.2.

To incorporate $\mathcal{S}(Z, z)$ directly extracted from the cosmological simulations, we implement a new method of modeling $\mathcal{S}(Z, z)$ in the **COMPAS** cosmic integration framework that constructs $\mathcal{S}(Z, z)$ from the TNG simulations (see Section 2.1). This method takes $\mathcal{S}(Z, z)$ as a two-dimensional array as a function of redshift and metallicity, along with the corresponding lookback times, redshifts, metallicity bin edges, and the binned metallicity distributions (dP/dlogZ) at each redshift. We then calculate the BBH properties across redshift following C. J. Neijssel et al. (2019); L. A. C. van Son et al. (2023); J. Riley et al. (2022). Our code is publicly available at S. Levina (2026). For the analytical fit, we perform the same method using the analytical fit $\mathcal{S}(Z, z)$ described in Section 2.2, which was already implemented

in the cosmic integration framework by L. A. C. van Son et al. (2023).

Once the merger rate weights have been computed, **COMPAS** provides access to the distributions of binary properties, such as masses, spins, formation redshifts, and formation metallicities of merging compact objects at any given redshift, which we will discuss in our results and compare to the GWTC-4 results from LIGO-Virgo-KAGRA (LVK) (The LIGO Scientific Collaboration et al. 2025). To study different evolutionary pathways, we classify binaries that experienced at least one common-envelope (CE) phase as CE-channel systems, and binaries that avoided CE evolution but underwent mass transfer as stable-channel systems.

We assess the accuracy of the analytical fit $\mathcal{S}(Z, z)$ by comparing it directly to $\mathcal{S}(Z, z)$ obtained from the TNG simulations, as well as by comparing the resulting BBH populations created with each $\mathcal{S}(Z, z)$ method. Specifically, throughout our work we compute the fit-to-simulation ratio for $\mathcal{S}(Z, z)$,

$$\frac{\text{fit } \mathcal{S}(Z, z)}{\text{simulation } \mathcal{S}(Z, z)}, \quad (7)$$

which quantifies where the fit overestimates or underestimates the simulated $\mathcal{S}(Z, z)$, as well as the fit-to-simulation ratio for the BBH merger properties,

$$\frac{\text{fit } d\mathcal{R}(z)/dx}{\text{simulation } d\mathcal{R}(z)/dx}, \quad (8)$$

which quantifies where the fit overestimates or underestimates the simulated BBH distribution (where dx can represent redshift dz or primary mass $dM_{\text{BH},1}$). We use this ratio rather than an absolute difference because the relevant quantities—such as $\mathcal{S}(Z, z)$, merger rate, and mass distribution—span several orders of magnitude. The ratio representation therefore provides a clearer measure of the fit quality across the parameter of interest.

3. RESULTS

3.1. Fit vs. simulation: Impact on $\mathcal{S}(Z, z)$

We fit the analytical $\mathcal{S}(Z, z)$ model to $\mathcal{S}(Z, z)$ extracted from the TNG simulations with different resolutions (see Section 2.1). The best-fit parameters are listed in Table 1, and Figure 1 compares the simulation $\mathcal{S}(z)$ to the corresponding analytical fits for the three TNGs used. Here, the simulation $\mathcal{S}(z)$ is computed by marginalizing TNG $\mathcal{S}(Z, z)$ over metallicity, while the analytical fits are produced using the best-fit parameters for $\mathcal{S}(z)$ in Equation (2).

The TNG simulation resolution primarily affects the normalization and peak location of $\mathcal{S}(z)$. TNG50-1,

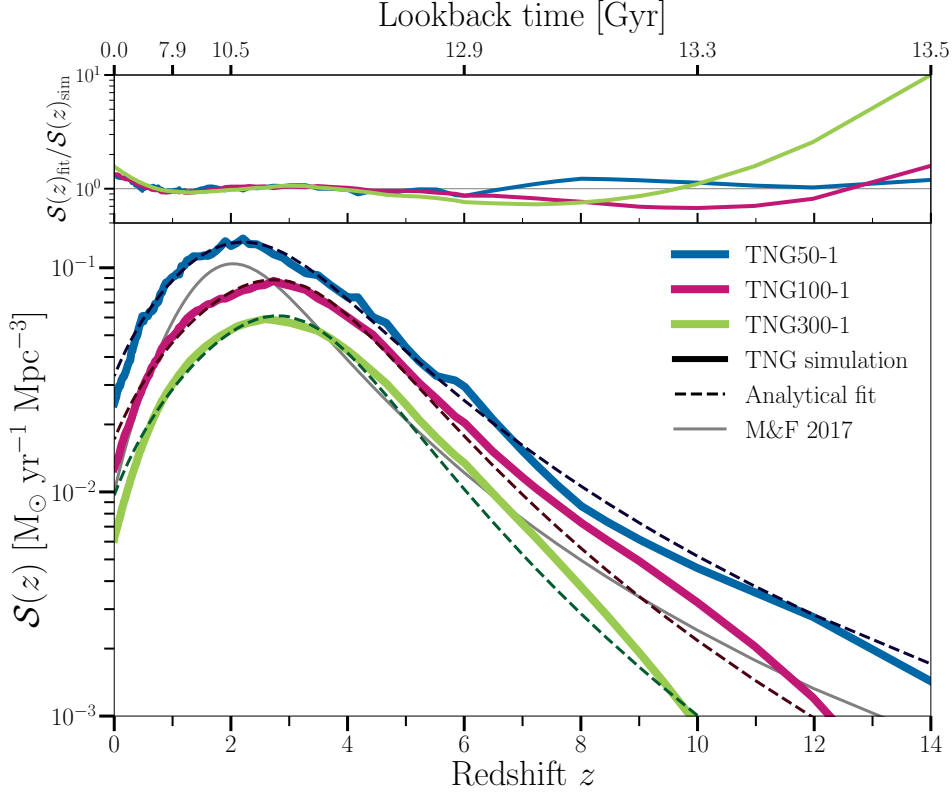


Figure 1. Bottom panel: Star formation rate density, $S(z)$, as a function of redshift, z , for the IllustrisTNG simulations TNG50-1 (blue), TNG100-1 (magenta), and TNG300-1 (green). Solid lines show $S(z)$ obtained by summing the full TNG $S(Z, z)$ from each simulation over metallicity, while dashed lines are analytical fits to the TNG $S(Z, z)$. For comparison, $S(z)$ model from P. Madau & T. Fragos (2017), which has the parameters $a = 0.01$, $b = 2.6$, $c = 3.2$, and $d = 6.2$ as defined in Equation (2), is shown as a gray line. **Top panel:** The fractional error for $S(z)$ as a function of redshift, as described in Section 2.4.

Table 1. Best fit $S(Z, z)$ parameters.

	TNG50-1	TNG100-1	TNG300-1
$dP/d\log Z$	μ_0	0.0282	0.0247
	μ_z	-0.0314	-0.0521
	ω_0	1.1136	1.1509
	ω_z	0.0592	0.0477
	α	-1.7353	-1.8801
$S(z)$	a	0.0329	0.0172
	b	1.4668	1.4425
	c	3.8412	4.5299
	d	5.0994	6.2261

with the highest mass resolution, yields the largest SFR at all redshifts, while TNG300-1, the lowest resolution run, is suppressed by roughly a factor ~ 2 . This change of normalization in the $S(Z, z)$ with numerical resolution is a well-known effect (see Appendix A of A. Pillepich et al. 2018a). This difference is encoded in $S(z)$ normalization parameter a , which decreases with resolution

(Table 1). Beyond the expected normalization change, the resolution also affects the redshift of peak star formation, where TNG50-1 peaks at $z \approx 2$, while TNG100-1 and TNG300-1 both peak near $z \approx 2.5$. The peak position is reflected in the parameter c , which emphasizes that the peak location of TNG50-1 differs from the other two simulations, which have approximately the same value of c . This may be an effect of the small box size and presence of a large cluster in TNG50-1, which might make TNG50-1 no longer representative of the “average” universe (A. Pillepich et al. 2019). The parameters b and d control the low- ($z \lesssim 2$) and high-redshift ($z \gtrsim 2$) slopes of $S(z)$, respectively. The low-redshift slope is fairly robust, but the analytical fit systematically overestimates $S(z)$ at $z \lesssim 0.5$ by up to a factor of ~ 1.5 . In contrast, the high-redshift slope varies strongly with resolution and shows a turning point near $z \approx 6-8$ that the analytical fit cannot reproduce (Figure 1). The fit over(under)estimates the high-redshift ($z \approx 6-12$) $S(z)$ by up to a factor of ~ 1.5 for TNG50-1 (TNG100-1 and TNG300-1). At $z \approx 14$, the fit overestimates $S(z)$ at all resolutions, by a factor of ~ 10 for TNG300-1 and ~ 2

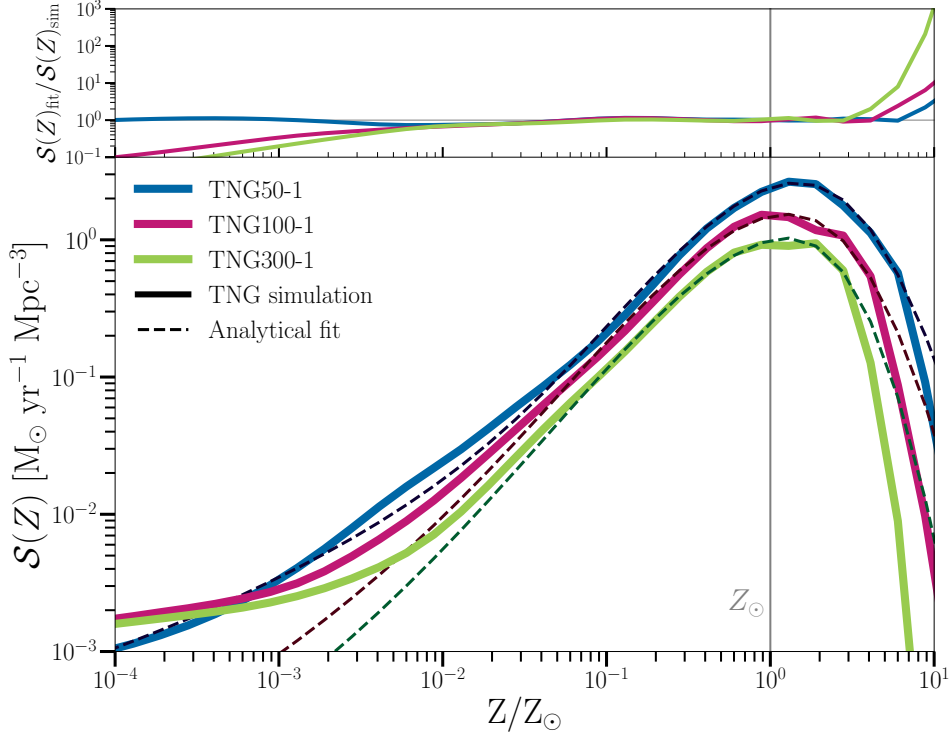


Figure 2. Bottom panel: Star formation rate density, $\mathcal{S}(Z)$, as a function of Z/Z_{\odot} . The colors and line styles are analogous to Figure 1. **Top panel:** The percent error for $\mathcal{S}(Z)$.

for TNG50-1 and TNG100-1. These effects may be a consequence of the optimization method, which prioritizes regions where the star formation rate is high (near the peak of star formation), and places less of an emphasis on regions in the parameter space where the star formation rate is low (e.g. at high redshift; see Sec 4.3).

We find that none of the TNG simulations align with the shape of the P. Madau & T. Fragos (2017) $\mathcal{S}(z)$ at all redshifts. Among the TNG runs, TNG100-1 aligns best with the P. Madau & T. Fragos (2017) $\mathcal{S}(z)$, consistent with the fact that the TNG simulations were calibrated at this resolution. However, the analytic form still fails to capture the steepening of the high- z tail ($z \gtrsim 6$) for all simulations.

Turning to metallicity, Figure 2 shows $\mathcal{S}(Z)$, obtained by integrating $\mathcal{S}(Z, z)$ over redshift. We find that the analytical fits fail to represent the full simulation $\mathcal{S}(Z)$ distributions. Agreement is best around $10^{-1} \lesssim Z/Z_{\odot} \lesssim 10^0$ but both the peak and the tails are poorly represented by the assumed skewed log-normal form in the analytical fit. The simulation-based $\mathcal{S}(Z)$ has one peak near $Z/Z_{\odot} \sim 1$ and an additional bump feature near $Z/Z_{\odot} \approx 2 - 5$ that the fit is unable to capture for all TNGs. The analytical fit instead locates a single peak at $Z/Z_{\odot} \approx 0.8 - 0$, increasing with resolution. Following the second peak in the simulation $\mathcal{S}(Z)$, there is a sharp drop-off. The fit overestimates $\mathcal{S}(Z)$ at $Z/Z_{\odot} \gtrsim 6$

by up to a factor of $\sim 10 - 1000$ depending on TNG resolution. At the low-metallicity end, TNG50-1 shows a change in slope between $10^{-3} \lesssim Z/Z_{\odot} \lesssim 10^{-2}$ (where $Z_{\odot} = 0.014$ M. Asplund et al. 2021), while TNG100-1 and TNG300-1 show a flattening for $Z/Z_{\odot} < 10^{-2}$. A more accurate analytical fit representation would require a steeper high-metallicity cutoff and a low-metallicity tail with at least one additional change in slope. We emphasize that the fit to $\mathcal{S}(Z, z)$ is performed in two dimensions, and the optimization may affect the quality of fit in any given dimension alone, as compared to fitting a skewed log-normal distribution to the metallicity distribution alone (see Section 4.3).

The full two-dimensional structure of TNG100-1 $\mathcal{S}(Z, z)$ is illustrated in Figure 3. We focus on TNG100-1 here, since it has intermediate resolution and box size and was the calibration resolution of the TNG suite (Section 2.1). We find that at super-solar metallicities, the analytical fit diverges increasingly from the simulation at low redshifts, due to a secondary bump in the simulation $\mathcal{S}(Z, z)$ that is smoothed over in the fit. This leads to alternating over- and underestimates of $\mathcal{S}(z)$ on the high metallicity end of the peak (see the right panel of Figure 3 above $Z/Z_{\odot} \gtrsim 1$). At the opposite end (low metallicity and high redshift) the analytical fit underestimates $\mathcal{S}(Z, z)$ compared to simulation, missing contributions at $Z/Z_{\odot} \lesssim 10^{-2}$ and $z \gtrsim 8$, as shown by

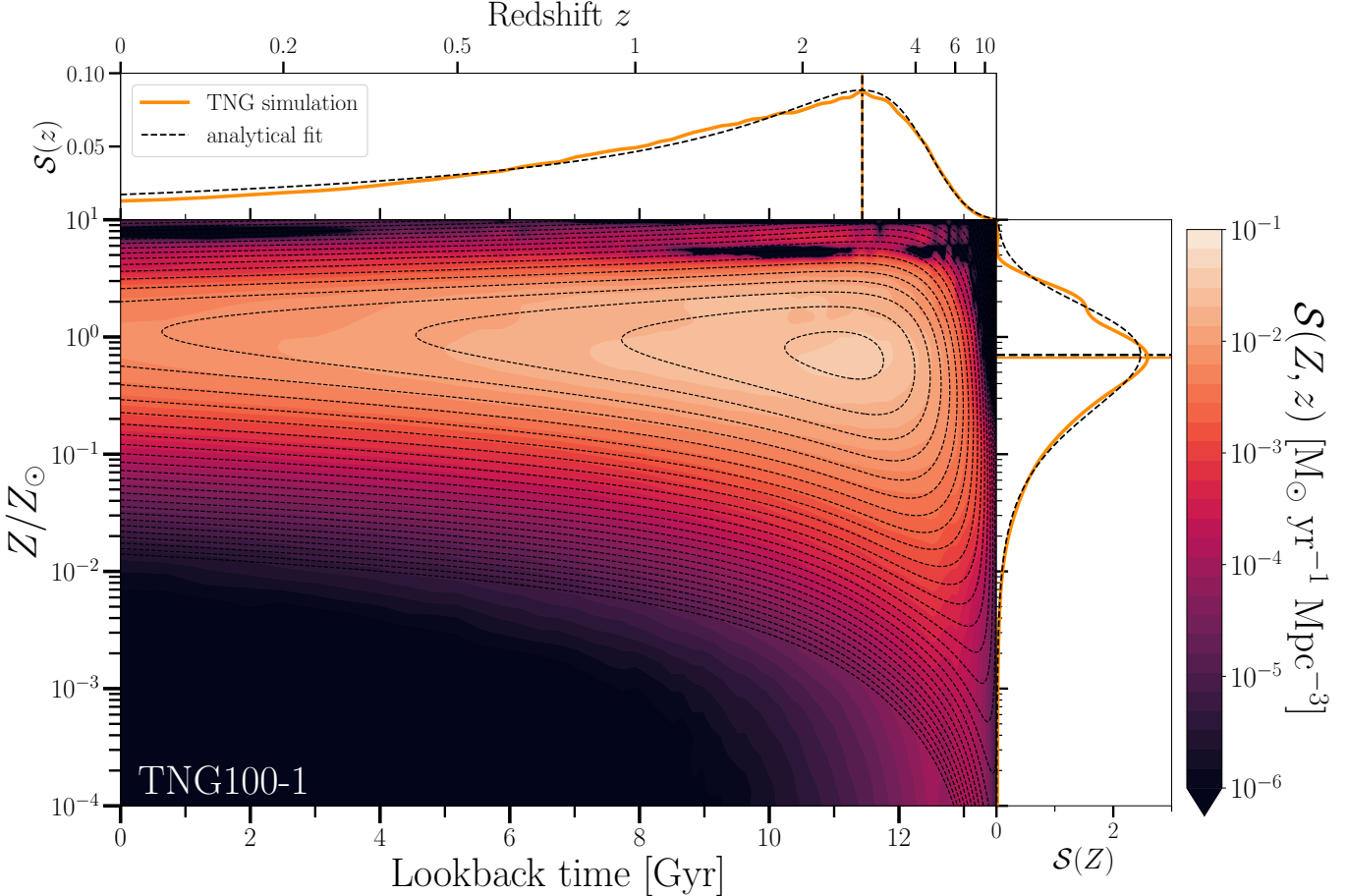


Figure 3. TNG100-1 $\mathcal{S}(Z, z)$ as a function of lookback time (Gyr) and Z/Z_{\odot} . The color bar shows the simulation $\mathcal{S}(Z, z)$ and the black dashed contours show $\mathcal{S}(Z, z)$ from the analytical fit. The top panel shows $\mathcal{S}(Z, z)$ marginalized over metallicity, and the right panel over lookback time. Note that the side panels are plotted using a linear scale for $\mathcal{S}(z)$ and $\mathcal{S}(Z)$. Black regions near the upper right reflect numerical noise from the interpolation edge.

the contours and in Figure 2, which is analogous to the right panel but using a logarithmic scale for $\mathcal{S}(Z)$ (see Appendix A). Note that there is a factor of ≈ 0.6 difference between the normalization of $\mathcal{S}(Z)$ plotted here as compared to Figure 2. This is likely a result of the interpolation of $\mathcal{S}(Z, z)$ in log-space (see Section 2.2) and its effects remain to be explored. The qualitative behavior of the fit remains the same.

While this regime is not critical for the BBH populations studied in Section 3.3.1, it may be important for studies focused on very low-metallicity star formation at early times.

3.2. Fit vs. simulation: Impact on the expected BBH merger rates

We now investigate how $\mathcal{S}(Z, z)$ obtained from different TNG simulations and analytical fits (Figure 1) influences the modeled BBH merger rates (calculated as in Section 2.3). Figure 4 shows the resulting BBH merger rate densities as a function of redshift, and Ta-

Table 2. Local merger rate at $z \approx 0$.

TNG version	$\mathcal{R}_{\text{sim}}(z)$ [Gpc 3 yr $^{-1}$]	$\mathcal{R}_{\text{fit}}(z)$ [Gpc 3 yr $^{-1}$]
50-1	58.92	73.72
100-1	42.91	45.53
300-1	29.34	27.81

ble 2 lists the corresponding local rates at $z \approx 0$. We find that the numerical resolution of the TNG simulations significantly affects both the amplitude and the redshift evolution of the expected BBH merger rate. At $z \approx 0$, the local merger rate varies from ~ 29 to ~ 59 Gpc $^{-3}$ yr $^{-1}$ between TNG300-1 and TNG50-1 when using the simulation $\mathcal{S}(Z, z)$, and from ~ 28 to ~ 74 when using the analytical fit. The merger rate peaks at $z \sim 2$ for TNG50-1 and at $z \sim 2.5$ for TNG100-1 and TNG300-1, similarly to the behavior of $\mathcal{S}(Z, z)$ (see Section 3.1). Near the peak, the merger rate in TNG50-1 exceeds that in TNG300-1 by roughly a factor of three (Figure 4). At

high redshift ($z \gtrsim 6$), the TNG50-1 merger rate is up to two orders of magnitude larger than in TNG300-1.

When using the analytical fit, the TNG50-1 merger rate at $z \approx 0$ is overestimated by about $15 \text{Gpc}^{-3} \text{yr}^{-1}$. For TNG100-1 and TNG300-1, the local rates from the simulation $\mathcal{S}(Z, z)$ and the fit agree within $\pm 2 \text{Gpc}^{-3} \text{yr}^{-1}$ (Table 2). The fit reproduces the merger-rate evolution most accurately between $z \approx 1\text{--}4$ for TNG50-1, $z \lesssim 2$ for TNG100-1, and $z \lesssim 1.5$ for TNG300-1. This behavior broadly reflects the quality of the fit to the underlying $\mathcal{S}(Z, z)$ (see Section 3.1). However, the deviations between fit and simulation at $z \lesssim 1$ are largely suppressed in the merger rate predictions, and the fit does not systematically overestimate or underestimate the $z \lesssim 1$ merger rates, likely due to the mixture of binaries with different delay times that formed at a range of redshifts. At high redshift ($z \gtrsim 6$), the analytical fits yield systematically larger BBH merger rates than those derived directly from the TNG simulation $\mathcal{S}(Z, z)$ —by factors of up to 10^4 for TNG300-1 and ~ 10 for TNG50-1 and TNG100-1 (Figure 4). Using the fit also leads to a shallower slope in the $z \gtrsim 4$ regime and a steeper decline in the merger rate toward $z \sim 14$.

3.3. Fit vs. simulation: Impact on BBH masses

We now investigate the impact of using the analytical fit versus simulation-based $\mathcal{S}(Z, z)$ on the primary mass distribution of BBHs in Figures 5, 6, and 7. Across redshifts and simulation/fit, the mass distributions typically show several key features: a steep incline from $\sim 5 M_\odot$ to a first local peak feature around $8 M_\odot$, followed by a further incline to a peak around $16 M_\odot$, a power law-like decline with an approximately consistent negative index between $16 M_\odot$ and $33 M_\odot$, and a further decline with an additional final local peak/mass feature around $45 M_\odot$. Combined, this results in (local) mass bump features around $M_{\text{BH},1} \approx 8 M_\odot$, a global maximum near $\sim 16 M_\odot$, and additional features at ~ 33 and $45 M_\odot$. These features are present across redshift, although their relative prominence varies. At higher redshifts ($z \gtrsim 2$), stochastic features appear for $M_{\text{BH},1} \gtrsim 30 M_\odot$ due to sampling.

We compare the contributions from the stable mass transfer and CE formation channels in Figure 5 (see Section 2.3), where we split the total (all channels) mass distribution into its stable and CE channel components. The main difference between the stable and CE mass distributions is that the $8 M_\odot$ feature is caused by the stable channel, while the $16 M_\odot$ peak and ~ 33 and $45 M_\odot$ features are dominated by the CE channel BBHs (Figure 5). The evolution across redshift is relatively

self-similar (Figure 6) with the rate increasing toward the peak of star formation near $z \approx 2$, followed by a decline towards higher redshift. The CE mass distribution at $\gtrsim 33 M_\odot$ increases with redshift, though both channels contribute to the high-mass features (Figure 5). The high-mass features are a result of pulsational-pair instability effects, and therefore appear in both channels (see Figure 6 of L. A. C. van Son et al. 2022b). The $33 M_\odot$ feature is an artificial feature produced by the switch between core-collapse supernova and pair pulsation prescriptions. The feature at $45 M_\odot$ is the pileup from pair-instability supernova.

The BBH mass distribution produced by the analytical fit shows significant deviations compared to the TNG simulation $\mathcal{S}(Z, z)$ that the fit is trying to represent. Most notably, at $z \lesssim 2$ (see Appendix B) the fit results in an artificial bump feature at $M_{\text{BH},1} \sim 8 M_\odot$ and suppresses both the high mass peaks, as shown in Figure 6. This excess rate is caused by the increase of the shoulder in the CE channel mass distribution at low masses (see the bottom two panels of Figure 5). At $\sim 8 M_\odot$, the fit results in a factor of $\sim 2\text{--}3$ greater BBH $d\mathcal{R}/dM$ for all TNG simulations a factor of $\sim 3\text{--}5$ lower at $M_{\text{BH},1} \gtrsim 35$ (Figure 7). The locations of the other mass features in the mass distribution produced using the analytical fit are more aligned with those that used the simulation $\mathcal{S}(Z, z)$.

We also find that the analytical mass distribution experiences less evolution in the overall rate for both the total distribution and both channels (consistent with Figure 4). Using the analytical $\mathcal{S}(Z, z)$ affects both channels. In the stable channel, the overall normalization of the mass distribution is overestimated, most prominently at higher redshift (Figure 5). In the CE channel, the $8 M_\odot$ feature is enhanced due the low-mass rate increasing with decreasing redshift until the low-mass peak is broadened into a plateau at $z = 0.2$.

Consistent with the results of Section 3.2, the rate decreases with simulation resolution, and there is no variation in the locations of mass features with TNG resolution. The analytical fit increasingly overestimates the rate across all masses as redshift increases, by up to a factor of $\sim 3, 4, 10$ at $z = 8$ for TNG50-1, TNG100-1, and TNG300-1, respectively (Figure 7).

3.3.1. Mass distribution as a function of formation metallicity and redshift

To investigate the origin of the artificial bump in the primary mass distributions around $8 M_\odot$ obtained using the analytical $\mathcal{S}(Z, z)$ fit (Figures 5 and 6), we examine the formation redshifts and metallicities of the binaries contributing to this feature for TNG100-1 to discern whether binaries forming in a specific region of $\mathcal{S}(Z, z)$

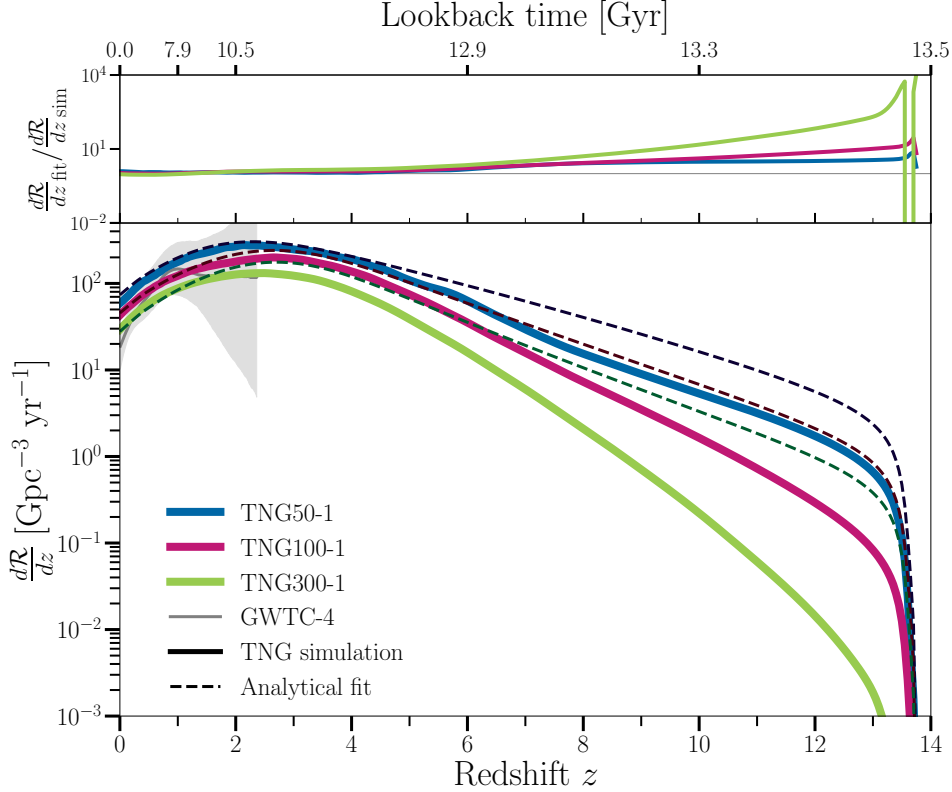


Figure 4. Bottom panel: BBH merger-rate density as a function of redshift. The observed BBH merger rate based on GWTC-4 data from [The LIGO Scientific Collaboration et al. \(2025\)](#) is shown in gray with the 95% credible regions. **Top panel:** the ratio between the rate from the analytical fit and TNG model (see Section 2.4). The noisy features in the ratio around $z \gtrsim 13$ arise from division by very small numbers. Colors and line styles match those in Figure 1.

contribute most to the excess rate near $8 M_{\odot}$. Figure 8 illustrates the contributions of different metallicities and formation redshifts to the BBHs mass distribution, with the corresponding ratios between the fit and simulation mass distributions for each bin in Figure 9. The regions of $\mathcal{S}(Z, z)$ corresponding to these metallicities and redshifts are shown in Figure 10.

We find that there is an excess of binaries with metallicities $0.01 \leq Z \leq 0.03$ (solid lines) in the total $z = 0.2$ mass distribution at $M_{\text{BH},1} \lesssim 15$ across all formation redshifts when using the analytical fit, compared to models using the full simulation $\mathcal{S}(Z, z)$ (Figure 9). The peak of the primary BH mass distribution in this metallicity range coincides with the artificial feature seen in the primary mass at $z_{\text{merger}} \lesssim 2$ (Figure 6). In contrast, the low metallicity (dotted lines; $10^{-4} \leq Z \leq 10^{-3}$) mass distributions are underestimated by the analytical fit by up to a factor ~ 10 at low formation redshift (light green lines; $0.2 \leq z_{\text{form}} \leq 0.5$) (Figure 9). The intermediate metallicity bin $10^{-3} \leq Z \leq 0.01$ (dashed lines) is least affected, showing discrepancies between fit and simulation of at most a factor of ~ 2 across all redshifts, as shown in Figure 9.

These trends indicate that the analytical fit overproduces high-metallicity ($Z \gtrsim Z_{\odot}$) BBHs, consistent with the poor performance of the analytical fit at high metallicity seen in Figure 10. The region corresponding to $0.01 \leq Z \leq 0.03$ (solid lines) across all redshifts contains the peak $\mathcal{S}(Z, z)$ values, and is where the analytical fit fails to reproduce the true $\mathcal{S}(Z, z)$ shape due to a secondary metallicity bump at high Z (Section 3.1). While COMPAS cannot produce binaries with $Z > 0.03$, the secondary bump causes the analytical fit to over-predict $\mathcal{S}(z)$ at $0.01 \leq Z \leq 0.03$ and affects the peak location of the metallicity distribution.

At high redshift and low metallicity, the analytical fit underestimates the fit to $\mathcal{S}(Z, z)$, leading to lower BBH merger rates and suppressed peaks in the high-mass end of the mass distribution (Section 3.1). Consequently, the contribution from the $10^{-4} \leq Z \leq 10^{-3}$ (dotted lines) metallicity bin drops by up to a factor ~ 2 . As shown in Figure 8, these low-metallicity populations span the full range of primary BH masses, but the over-prediction of higher metallicity systems at $M_{\text{BH},1} \lesssim 20$ makes the discrepancy most prominent at higher masses. The intermediate metallicity bin $10^{-3} \leq Z \leq 10^{-2}$

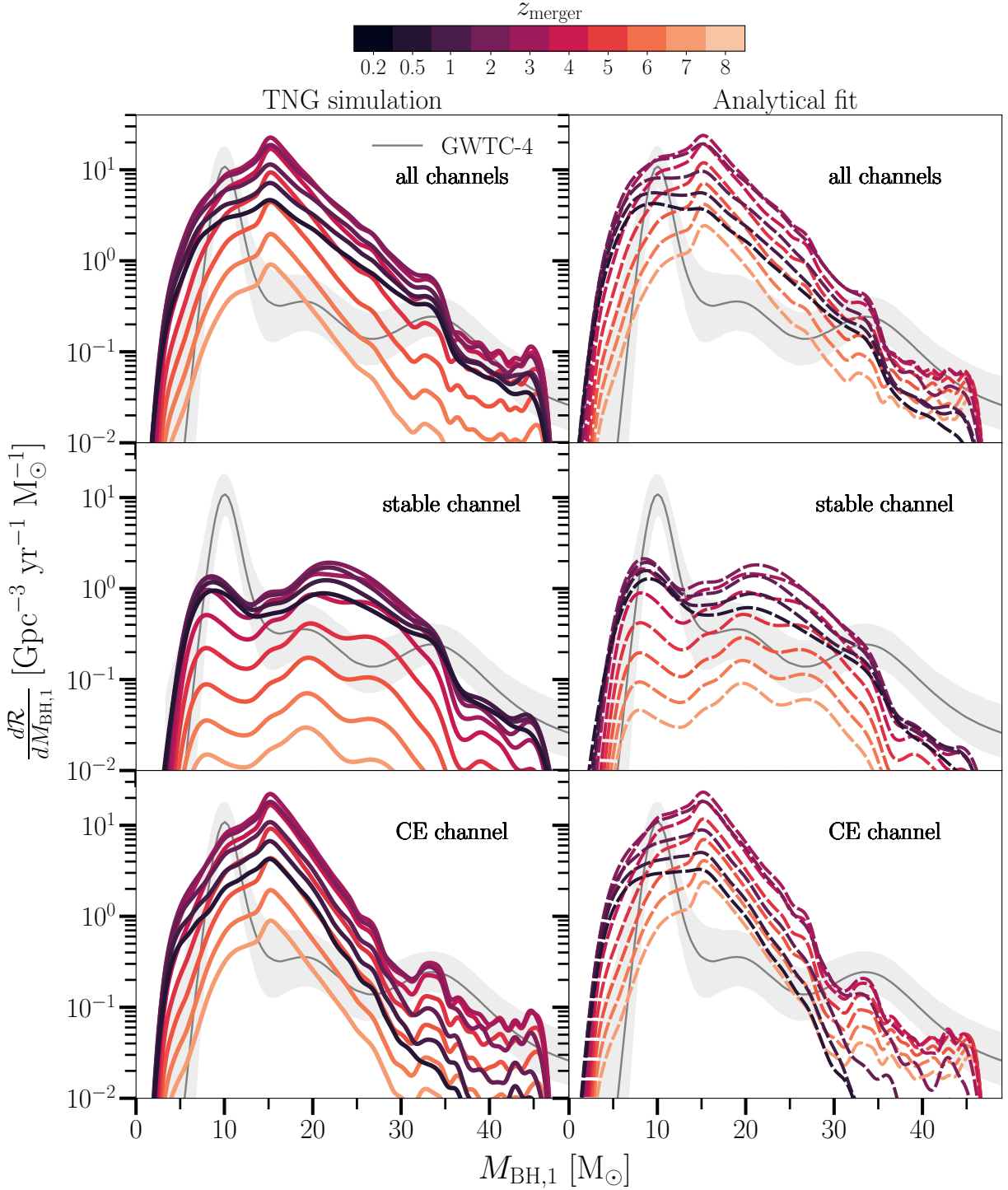


Figure 5. Redshift evolution of the BBH primary mass distribution, $M_{\text{BH},1} [\text{Gpc}^{-3} \text{yr}^{-1} \text{M}_\odot^{-1}]$, for the TNG100-1, computed using the full simulation $\mathcal{S}(Z, z)$ (left column) and the analytical fit (right column). The darkest color represents the local mass distribution $z_{\text{merger}} = 0.2$ and the lightest is at $z_{\text{merger}} = 8$. The B-spline BBH primary mass distribution from GWTC-4 (The LIGO Scientific Collaboration et al. 2025) is shown in gray. The rows represent different formation channels: the top row includes mergers from both the stable mass transfer and common-envelope (CE) channels, the middle row shows only stable mass transfer channel mergers, and the bottom row includes only CE channel mergers.

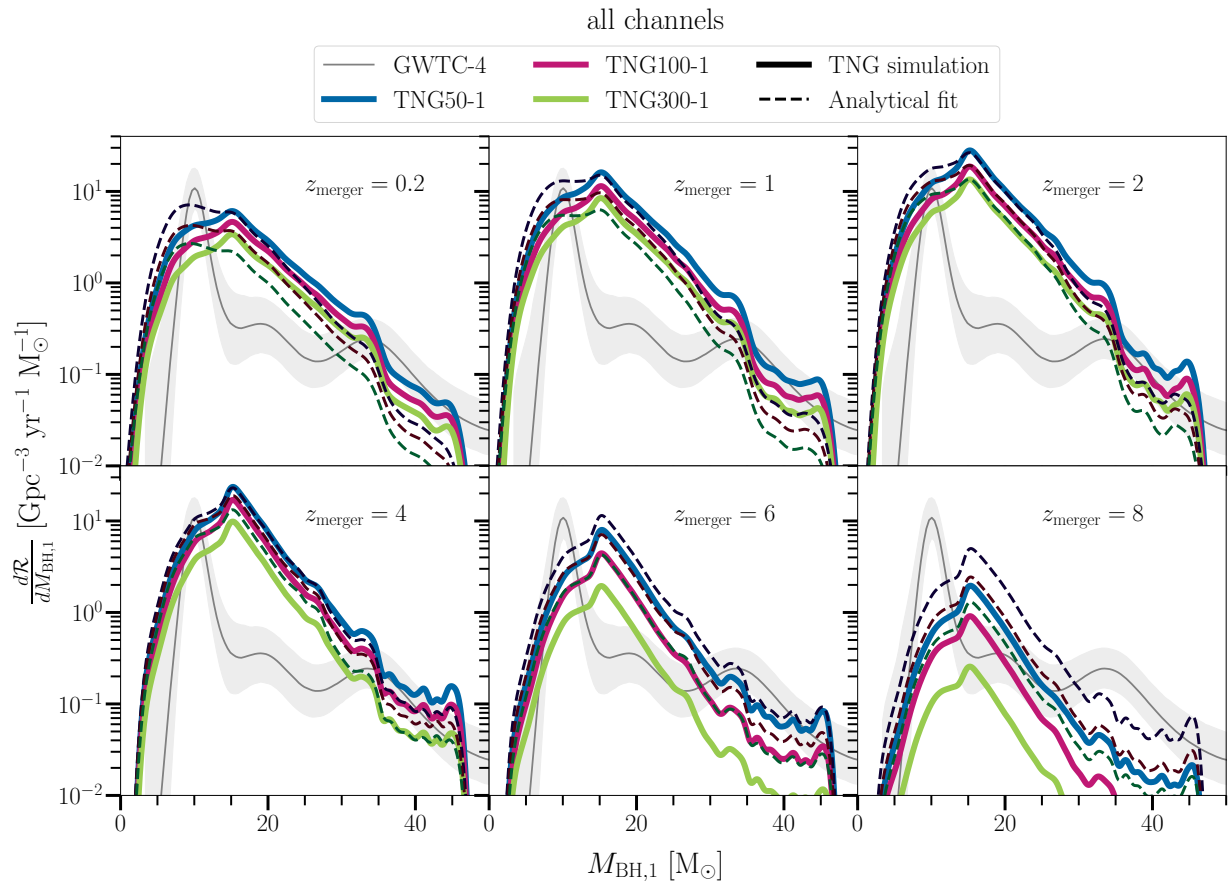


Figure 6. Comparison of BBH primary mass distributions (in units of $\text{Gpc}^{-3}\text{yr}^{-1}\text{M}_\odot^{-1}$) for the TNG simulations. The colors and line styles are the same as in Figure 1. For reference, the observed local BBH primary mass distribution at $z_{\text{merger}} = 0.2$ from GWTC-4 (The LIGO Scientific Collaboration et al. 2025) is shown in gray. The panels show the mass distributions for redshifts $z_{\text{merger}} = 0.2, 1, 2, 4, 6, 8$.

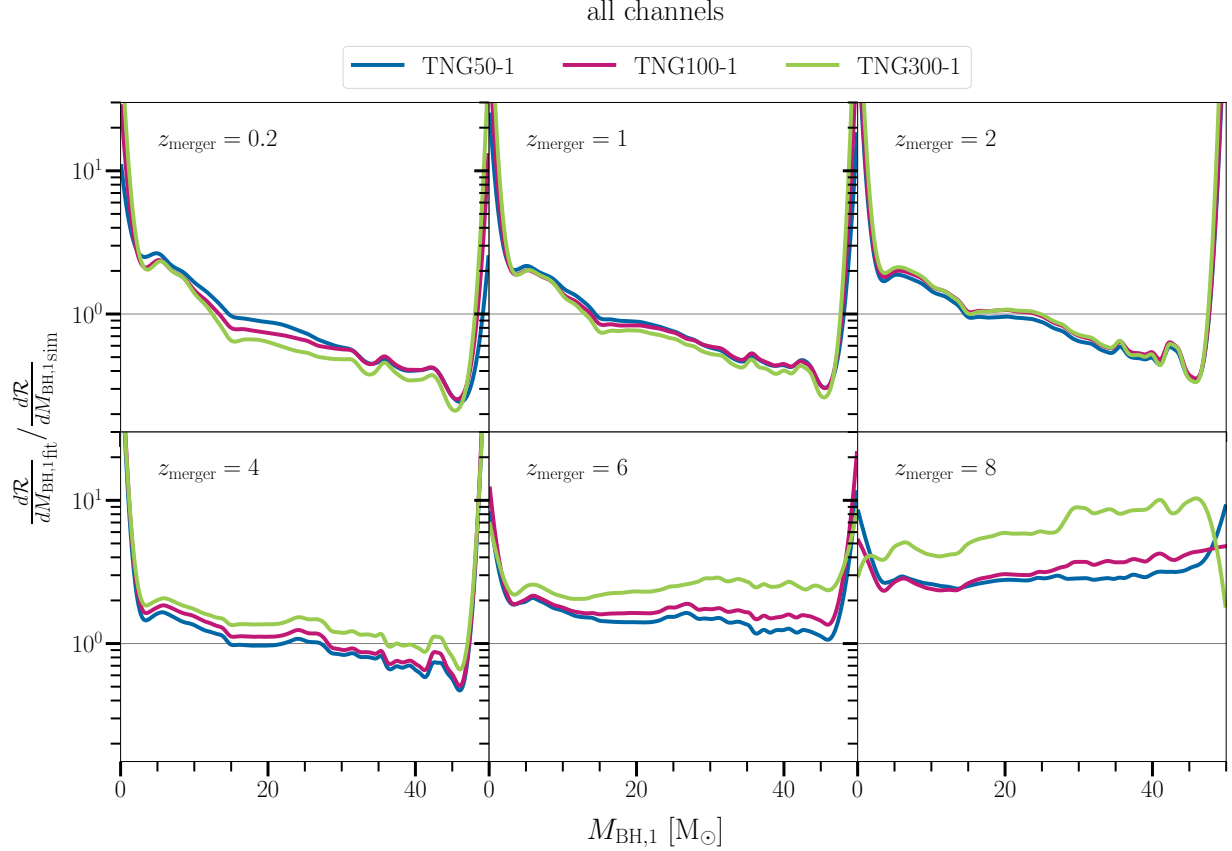


Figure 7. The ratio between the fitted BBH primary mass distributions and those from the TNG simulations for $z_{\text{merger}} = 0.2, 1, 2, 4, 6, 8$. Note that the ratio at the edges should not be trusted due to the boundaries of the mass distributions.

(dashed lines) remains relatively unaffected across most redshifts, though it shows an increased contribution (by about a factor 2) at the highest redshifts ($6 \lesssim z \lesssim 10$).

We therefore caution that models relying on analytical $\mathcal{S}(Z, z)$ fits may be unreliable, especially when considering contributions from populations originating at high redshift ($z \gtrsim 6$) and low metallicity ($Z/Z_{\odot} \lesssim 10^{-2}$). Improving the fit to $\mathcal{S}(Z, z)$ in both the high metallicity-low redshift and the low metallicity-high redshift regime is essential, since a substantial fraction of binaries merging at $z_{\text{merger}} = 0.2$ form in these regions. Future analytical fits should allow for more flexible modeling of the metallicity distribution—potentially incorporating a secondary high-metallicity peak and a flatter low-metallicity tail—to better capture the structure of $\mathcal{S}(Z, z)$.

4. DISCUSSION

4.1. Comparison to earlier work investigating the impact from $\mathcal{S}(Z, z)$ on BBH populations

4.1.1. Analytical fit $\mathcal{S}(Z, z)$

Analytical fits are a convenient means of representing cosmological simulation $\mathcal{S}(Z, z)$ distributions due to

their computational simplicity and the ability to quantify $\mathcal{S}(Z, z)$ uncertainties using physically-motivated parameters. Earlier work has explored the impact from using analytical fits for $\mathcal{S}(Z, z)$ assumptions on double compact object merger populations. C. J. Neijssel et al. (2019) explored the impact of $\mathcal{S}(Z, z)$ using analytical fits, using a parametrized prescription that combines the P. Madau & M. Dickinson (2014) functional form for $\mathcal{S}(z)$ with a log-normal metallicity distribution derived from the GSMF and MZR. The authors obtain a “preferred model” by best-fitting analytical fit parameters from BBH observations from the first two observing runs of LVK. They compare this against models for $\mathcal{S}(z)$, GSMF, and MZR from galaxy observations (B. Panter et al. 2004; S. Savaglio et al. 2005; N. Langer & C. A. Norman 2006) or cosmological simulations (M. Furlong et al. 2015; X. Ma et al. 2016). They find a BBH rate for the preferred model that is about an order of magnitude lower than those produced using the other (analytical, but observation-based) models, which is attributed to the “preferred” model having larger metallicities at low redshift, which decreases the BBH yield at low redshift. The C. J. Neijssel et al. (2019) analytical form and fit pa-

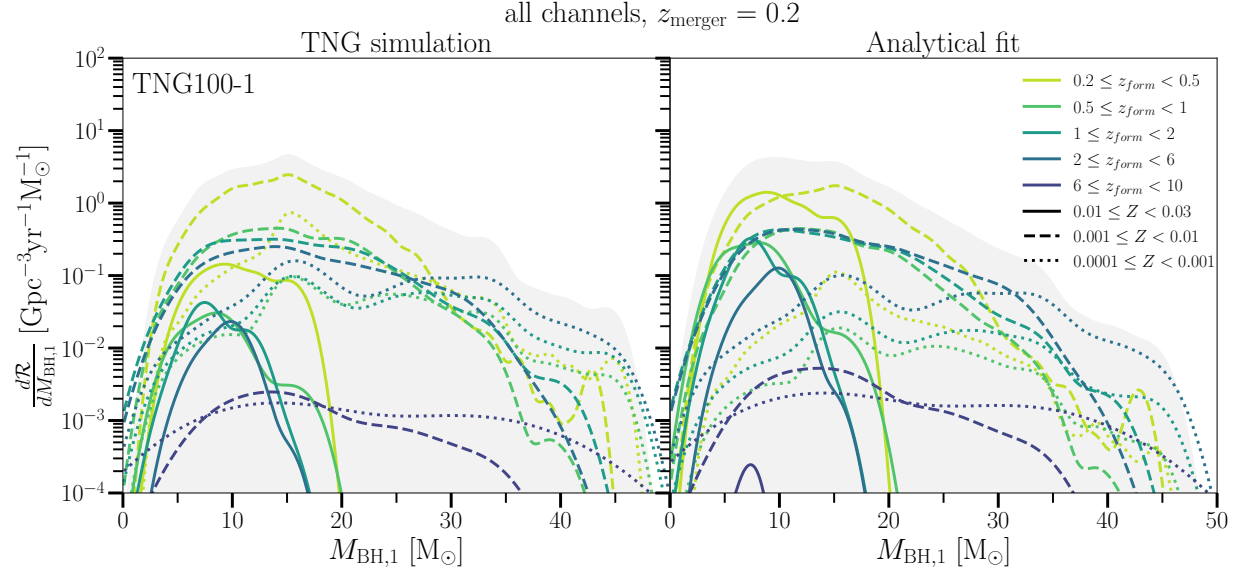


Figure 8. The $z_{\text{merger}} = 0.2$ BBH primary mass distribution for TNG100-1 using $\mathcal{S}(Z, z)$ from the simulation (left) and the analytical fit (right), binned by formation redshift (color) and metallicity (line style). The solid lines represent the highest metallicity bin ($0.01 \leq Z < 0.03$), the dashed line represent the $0.001 \leq Z < 0.01$ bin, and the dotted line is the lowest metallicity bin ($0.0001 \leq Z < 0.001$). The gray shading represents the total rate, and the behavior at the edges is attributed to the use of KDEs in plotting the mass distribution. The bins cover the full parameter space of binaries in our population that merge at $z_{\text{merger}} = 0.2$.

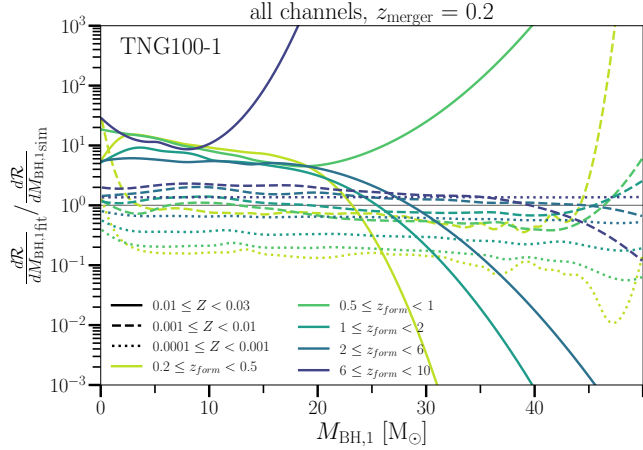


Figure 9. The ratio between the fit and simulation mass distributions, binned by metallicity and formation redshift. The colors and line styles are analogous to Figure 8. The behavior of the low metallicity (solid) distribution ratios at $M_{\text{BH}, 1} \gtrsim 15$ are due to their very small rates in that regime.

rameters are a widely used $\mathcal{S}(Z, z)$ model (e.g., J. Riley et al. 2022; S. Stevenson et al. 2019; J. Riley et al. 2021; F. S. Broekgaarden et al. 2022; L. A. C. van Son et al. 2022b, 2023; I. Romero-Shaw et al. 2023; S. K. Roy et al. 2025). However, M. Chruścińska (2024) showed that the preferred model of C. J. Neijssel et al. (2019) is unphysical due to the negligible low-metallicity star formation at $z \lesssim 2$, and the resulting BBH rates deviate signifi-

cantly from the rates produced using observational and cosmological simulation $\mathcal{S}(Z, z)$ assumptions.

M. M. Briel et al. (2022) model metallicity-dependent transient rates (including BBH mergers) using the TNG100-1, EAGLE (J. Schaye et al. 2015), and Millennium (V. Springel et al. 2005) cosmological simulations. They compare the full $\mathcal{S}(Z, z)$ from each simulation to an empirical analytical model combining the P. Madau & M. Dickinson (2014) $\mathcal{S}(z)$ with the N. Langer & C. A. Norman (2006) metallicity distribution. While the simulations broadly agree at $z \lesssim 2$, they diverge at higher redshifts. Consistent with our findings, none of the simulation $\mathcal{S}(Z, z)$ are well-represented by the empirical model; in particular, the high-redshift slope deviates substantially from a P. Madau & M. Dickinson (2014) form. Moreover, the N. Langer & C. A. Norman (2006) metallicity prescription does not reproduce the metallicity distributions found in cosmological simulations. The resulting BBH merger rates in M. M. Briel et al. (2022) vary by nearly an order of magnitude, with the peak location spanning between $1.5 \lesssim z \lesssim 3$, depending on the cosmological simulation used. They conclude that metallicity-dependent transients with long delay times, such as BBH, are most sensitive to $\mathcal{S}(Z, z)$ assumptions, attributed primarily to differences in the metallicity distribution and its redshift evolution, which are not captured by the N. Langer & C. A. Norman (2006) model. Their BBH merger rate based on TNG100-1 is consis-

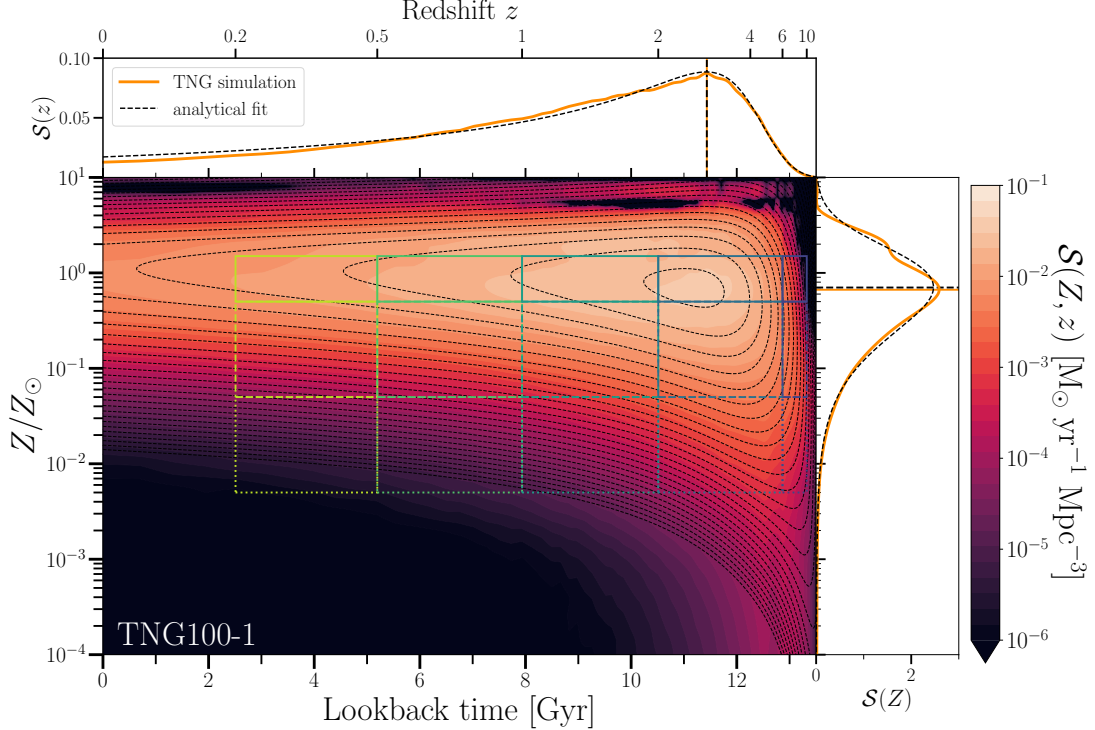


Figure 10. Analogous to Figure 3, but with the metallicity and redshift bins used in Figure 8 plotted as rectangles. Note that the maximum COMPAS metallicity is $Z = 0.03$.

tent with our results using the full TNG100-1 $\mathcal{S}(Z, z)$, including at $z \approx 0$, despite differences in population synthesis model (BPASS versus COMPAS).

L. A. C. van Son et al. (2023) create an analytical fit for $\mathcal{S}(Z, z)$ model based on the TNG100-1 simulation—this is the work that our paper builds forward on. In this paper the authors focus on investigating the performance of the analytical fit as a proxy for the TNG100-1 simulation $\mathcal{S}(Z, z)$ by comparing the accuracy for $\mathcal{S}(Z, z)$ (but not the BBH populations.) The work builds on the approach from C. J. Neijssel et al. (2019), but allows for a skewed log-normal metallicity distribution with a low-metallicity tail in $\log_{10} Z$. Their analytical fit is able to capture the large-scale behavior of the TNG100-1 $\mathcal{S}(Z, z)$, but similarly fails to fit a secondary bump in $\mathcal{S}(z)$ (see the bottom left panel of their Figure 1). The authors additionally investigate how changing the analytical fit parameters impacts the BBH population. They find that there is little variation in the locations of major features in the BBH primary mass distribution over variations in $\mathcal{S}(Z, z)$ parameters. Similarly, we find that locations of major features are consistent across TNG version and redshift (see Figures 5-6). L. A. C. van Son et al. (2023) find that the low-mass end of the BBH mass distribution is least affected by $\mathcal{S}(Z, z)$, while the high-mass end is most affected by parameters that describe the redshift evolution of $\mathcal{S}(Z, z)$. We find

that both the low-mass peak and high-mass end of the mass distribution is affected by the redshift evolution of $\mathcal{S}(Z, z)$ (see Figure 6).

Their $z = 0.2$ merger rates for the stable and CE channels are 17.1 and 41.8 mergers $\text{Gpc}^{-3} \text{yr}^{-1}$, respectively, when using the fiducial $\mathcal{S}(Z, z)$. Depending on $\mathcal{S}(Z, z)$ parameter variations, the merger rates range between $6.3 - 65.4 \text{ Gpc}^{-3} \text{yr}^{-1}$ for the stable channel and $24.2 - 144.1 \text{ Gpc}^{-3} \text{yr}^{-1}$ for the CE channel. Our merger rates for all three TNG versions are approximately within the total range found by L. A. C. van Son et al. (2023), though on the lower end, as we calculate the merger rate at $z \approx 0$ rather than $z = 0.2$. For the fitted TNG100-1 $\mathcal{S}(Z, z)$, we find a total rate of $45.53 \text{ Gpc}^{-3} \text{yr}^{-1}$ at $z \approx 0$ (see Table 2). Minor differences in fit values likely arise from differing cosmological parameters (we adopt Planck 2016 to match TNG, while L. A. C. van Son et al. (2023) use Planck Collaboration 2020) and differences in assumed onset redshift of star formation ($z = 14$ in our COMPAS setup versus $z = 10$ in L. A. C. van Son et al. 2023).

A similar analysis to this work should be extended to other cosmological simulations in order to verify whether other $\mathcal{S}(Z, z)$ distributions may be more reasonably represented by analytical prescriptions than TNG. If this is the case, improvements of the analytical fit could be explored. This may include features such as allowing

for a secondary, redshift-dependent peak in the metallicity distribution and greater flexibility for changes in slope within the low-metallicity tail. Improvements in optimization methods should also be explored, as they must balance between an accurate fit to the peak of star formation and the low-metallicity tail of the metallicity distribution.

4.1.2. *Simulation-based $\mathcal{S}(Z, z)$*

Cosmological simulations have also been directly (i.e., without using a fit) used in population synthesis studies of GW sources. This method avoids constructing an explicit $\mathcal{S}(Z, z)$: BBHs formed in population synthesis are associated with newly formed star particles of similar metallicity, and their merger time is derived from the formation redshift and delay time. For example, [M. Mapelli et al. \(2017, 2019\)](#) calculate BBH merger rates via Monte Carlo placement of BBH systems simulated using a population synthesis model using **MOBSE** ([N. Giacobbo et al. 2018](#)), an updated version of the **BSE** code ([J. R. Hurley et al. 2000, 2002](#)), onto star particles in cosmological simulations. Using the **Illustris-1** simulation ([M. Vogelsberger et al. 2014](#)), [M. Mapelli et al. \(2017\)](#) find local BBH merger rates typically an order of magnitude higher than ours, attributable to differences in binary physics rather than $\mathcal{S}(Z, z)$ assumptions. [M. Mapelli et al. \(2019\)](#) find minimal redshift evolution in the mass distribution across several binary evolution variations, which is attributed to BBHs from low-metallicity ($Z \lesssim 4 \times 10^{-3}$) dominating the BBH population across redshift.

[M. C. Artale et al. \(2019, 2020\)](#) apply a similar method to the **EAGLE** simulations to explore the BBH merger rate per galaxy and its dependence on galaxy mass, SFR, and metallicity. They find that the stellar mass of a galaxy is the strongest tracer of the double compact object merger rate per galaxy. [M. C. Artale et al. \(2020\)](#) show that specific SFR variations (where the specific SFR is the SFR/galaxy stellar mass) can cause order of magnitude variations in the BBH merger rate. Our values for the local merger rate given the **TNG** $\mathcal{S}(Z, z)$ variations fall within that range.

[F. Marinacci et al. \(2025\)](#) incorporate double compact object calculations directly into the moving-mesh code **AREPO** (both on-the-fly and in post-processing). They demonstrate their approach using **MillenniumTNG** and explore how box size affects $\mathcal{S}(Z, z)$ and the resulting BBH populations, finding minimal sensitivity to simulation volume. While on-the-fly modeling has conceptual advantages, the computational cost likely limits parameter exploration relative to post-processing methods.

4.1.3. *Alternative $\mathcal{S}(Z, z)$ models*

The GW source populations have also been modeled using observational galaxy scaling relations with **GalaxyRate** ([F. Santoliquido et al. 2022](#)) for $\mathcal{S}(Z, z)$ and **SEVN** ([M. Spera & M. Mapelli 2017; M. Spera et al. 2019](#)), including variations in the **GSMF** ([M. Chruścińska & G. Nelemans 2019](#)), galaxy main sequence ([J. S. Speagle et al. 2014; L. A. Boogaard et al. 2018; P. Popesso et al. 2023](#)), and metallicity relations ([F. Mannucci et al. 2011; B. H. Andrews & P. Martini 2013; M. Curti et al. 2020](#)). These authors model $\mathcal{S}(Z, z)$ analytically following [P. Madau & T. Fragos \(2017\)](#) and a redshift-dependent metallicity spread using **CosmoRate** ([F. Santoliquido et al. 2020](#)). The resulting BBH merger rates vary by about an order of magnitude across model variations and generally exceed the observed rate ([The LIGO Scientific Collaboration et al. 2025](#)). They find that binary evolution assumptions have stronger impact on BBH rates than $\mathcal{S}(Z, z)$ variations, and that analytical $\mathcal{S}(Z, z)$ models can mimic more detailed galaxy-based ones when allowing a large metallicity spread. Their BBH rates exceed ours (based on **TNG** and **COMPAS**) by roughly an order of magnitude. Whether population synthesis differences alone can explain the rate offset, or whether cosmological simulations underpredict the BBH rate relative to observation-based models, remains an open question.

A direct comparison of our results with observational $\mathcal{S}(Z, z)$ distributions, such as those derived by [M. Chruścińska & G. Nelemans \(2019\)](#), would identify whether the features where the analytical fit fails for **TNG** also exist in observations. If those common features exist, this would emphasize the need to move away from representing star formation histories using $\mathcal{S}(Z, z)$ and constrain the behavior and parameter space that realistic $\mathcal{S}(Z, z)$ should span.

4.2. *Effects from cosmological simulations and binary evolution modeling*

4.2.1. *Resolution effects*

In this work, we showed the effects of resolution on the **IllustrisTNG** $\mathcal{S}(Z, z)$, but future studies should investigate this in greater detail, combined with box sizes effects and for other simulations.

Cosmological simulations are calibrated to match a subset of scaling relations. The choice of relations and the degree of allowed freedom varies across simulation suites. **IllustrisTNG**, for example, was calibrated to reproduce the redshift evolution of the star formation rate density, the $z \approx 0$ **GSMF**, the black hole mass–stellar mass relation, the galaxy size–mass relation, and the stellar-to-halo mass (**SMHM**) relation ([A. Pillepich et al.](#)

2018a), with some flexibility. In contrast, EAGLE simulations (J. Schaye et al. 2015) were calibrated primarily to reproduce the SMHM relation with additional constraints from the GSMF, galaxy size-mass relation, and black hole scaling relations.

Most cosmological simulation suites include multiple runs with varying resolution. In a given simulation, gas cell masses span a factor of ~ 2 around the target mass resolution (A. Pillepich et al. 2018a). IllustrisTNG exhibits a $\sim 30\%$ systematic shift in stellar mass for each factor-of-eight change in mass resolution at fixed halo mass (see Appendix A of A. Pillepich et al. 2018a). As the TNG simulations were calibrated at the TNG100-1 resolution, the higher-resolution TNG50-1 produces excess star formation and therefore a higher $\mathcal{S}(Z, z)$ normalization.

This reflects IllustrisTNG’s use of strong resolution convergence: parameters are not recalibrated at higher resolution, preserving numerical and physical consistency across runs but not compensating for resolution-driven changes in subgrid physics (A. Pillepich et al. 2018a). F. Marinacci et al. (2014) find that strong convergence across resolution leads to more consistent galaxy properties in some contexts. By contrast, the EAGLE simulations adopt weak resolution convergence, recalibrating subgrid parameters at higher resolution to minimize systematic shifts (J. Schaye et al. 2015). Whether weak or strong convergence is preferable depends on which scaling relations were used for the (re)calibration. A systematic comparison of weak versus strong convergence effects on $\mathcal{S}(Z, z)$ and BBH populations remains unexplored.

Evaluating the performance of the analytical $\mathcal{S}(Z, z)$ model as an approximation of the TNG simulations is the first step of investigating the effect of star formation histories on BBH populations across different cosmological simulations. Subsequently, we will perform an in-depth study of the effects of resolution and simulation box volume on $\mathcal{S}(Z, z)$ and the resulting BBH merger population.

A more complete treatment would move beyond galaxy-averaged $\mathcal{S}(Z, z)$ to include spatial gradients and scatter in metallicity and SFR within galaxies, accessible through zoom-in simulations such as FIRE and FIREbox (P. F. Hopkins et al. 2023; R. Feldmann et al. 2023). Such inhomogeneities, typically washed out in global averages, may create localized sites of massive-star formation that are disproportionately important for producing GW progenitors. Extending this work to characterize the host environments of isolated GW sources, including the masses, types, and internal regions of galaxies

contributing most to progenitor formation, will also enable future multi-messenger applications.

4.2.2. Population synthesis models

In this work, we use a single binary evolution model from COMPAS, which may affect the results quantitatively, as binary evolution contributes substantial uncertainties to the resulting population. Processes such as common envelope evolution can alter merger rates by more than an order of magnitude across models (e.g. A. Olejak et al. 2021; F. S. Broekgaarden et al. 2022), with uncertainties increasing at the highest BBH masses (e.g. A. Romagnolo et al. 2023). While there is active research ongoing to use detailed binary models to refine prescriptions (e.g. P. Marchant et al. 2021; A. Romagnolo et al. 2025), rapid population synthesis codes necessarily rely on simplified assumptions to remain computationally tractable. Both M. Mapelli et al. (2017) and C. Sgalletta et al. (2024) find that binary evolution uncertainties often dominate over $\mathcal{S}(Z, z)$ uncertainties in their impact on BBH merger rates. The BBH rates may be overestimated due to the large BBH formation efficiencies in population synthesis codes, where 1 in 8 binaries that have a high enough mass to form a BBH will form a merging BBH (L. A. C. van Son et al. 2025). Additionally, the authors suggest that BBH formation efficiency may not be nearly as strongly metallicity-dependent as shown by previous works, due to updated wind prescriptions, and the degree of importance of metallicity may be formation channel dependent. Future work should further explore $\mathcal{S}(Z, z)$ and binary modeling effects for other binary population synthesis codes, formation channels, and model variations.

4.3. Effects from fit optimization

In addition to effects arising from cosmological simulation resolution and binary population modeling, the optimization of the analytical fit to $\mathcal{S}(Z, z)$ can also have a significant impact. The choice of optimization strategy affects the quality of the fit and, therefore, the accuracy with which the analytical fit parameters represent $\mathcal{S}(Z, z)$ for BBH population modeling. In this work, we adopt the cost function described in L. A. C. van Son et al. (2023), which is designed to balance an accurate representation of both the peak of star formation and the high-redshift, low-metallicity tails where $\mathcal{S}(Z, z)$ is low. Because the high-redshift and low-metallicity regimes of $\mathcal{S}(Z, z)$ are particularly critical for the formation of merging BBH systems, a penalization factor is applied to reduce the contribution of the star formation peak to the fit. This prevents the optimization from being dominated by the high values of $\mathcal{S}(Z, z)$ near $z \sim 2$. Nevertheless, the analytical fit performs poorly at high

redshift (Figure 1 and 3) and at both low and high metallicities (Figure 2 and 3), where $\mathcal{S}(Z, z)$ is intrinsically low. In particular, the analytical fit fails to capture the bimodality of $\mathcal{S}(Z)$ and the truncation of the low-metallicity tail; features that both affect the resulting BBH mass distribution (see Section 3.3.1). While these limitations are inherent to the functional form of the analytical fit, improvements to the optimization strategy should nonetheless be explored to improve the accuracy of reproducing the $\mathcal{S}(Z, z)$ using an analytical fit. For the optimization itself, we use the BFGS algorithm (J. Nocedal & S. Wright 2006) for TNG50-1 and TNG100-1 simulations, and the Nelder-Mead method (F. Gao & L. Han 2012) for TNG300-1. The latter choice is motivated by the failure of BFGS to converge for TNG300-1, possibly due to the bimodality of $\mathcal{S}(Z)$. The sensitivity of the results to the choice of optimization algorithm should therefore also be investigated in the future.

5. CONCLUSIONS

We model the BBH merger population using both the star formation histories of the three IllustrisTNG cosmological simulations of varying resolution and volume (TNG50-1, TNG100-1, and TNG300-1) and analytical fits to each simulation in order to explore the effectiveness of analytical models in representing a more detailed, underlying $\mathcal{S}(Z, z)$ when modeling BBH populations. All populations are modeled using the same COMPAS binary population synthesis simulations from L. A. C. van Son et al. (2022b) and L. A. C. van Son et al. (2022a), which we then combine with $\mathcal{S}(Z, z)$ using the COMPAS “cosmic integration” post-processing tool. To do this, we develop a new method of performing cosmic integration using $\mathcal{S}(Z, z)$ as a 2-D (rather than separate $\mathcal{S}(z)$ and metallicity distribution), such as that which can be derived from a cosmological simulation or observational data. We test whether using an analytical form that combines the Madau & Dickinson form of $\mathcal{S}(z)$ with a skewed log-normal metallicity distribution is a reliable approximation for the full $\mathcal{S}(Z, z)$ of each TNG simulation when considering the impact on the resulting BBH population properties.

We find that the analytical $\mathcal{S}(Z, z)$ model fails to accurately represent $\mathcal{S}(Z, z)$ of the TNG simulations. The fit is unable to capture the shape of $\mathcal{S}(Z, z)$ at $Z \gtrsim Z_{\odot}$, missing a secondary bump in the metallicity distribution near $3Z_{\odot}$. As the fit attempts to smooth over this feature, it falsely locates the global maximum of the metallicity distribution at a higher metallicity than in the simulation $\mathcal{S}(Z, z)$. This produces a nontrivial effect on the resulting BBH merger population. When using the analytical fit to model $\mathcal{S}(Z, z)$:

1. The high-redshift ($z \gtrsim 4$) BBH merger rate is overestimated by up to a factor of $10 - 10^4$, depending on simulation resolution. This effect becomes more prominent with increasing redshift and decreasing TNG resolution.
2. With decreasing resolution, the merger rate peaks at higher redshift.
3. There is an artificial excess $8 M_{\odot}$ feature at in the $z_{\text{merger}} = 0.2$ primary mass distribution, by up to a factor of 7 at $z_{\text{merger}} \lesssim 2$. This feature may primarily originate from the CE channel.

However, the locations of features in the primary mass distribution remain consistent across fit and simulation $\mathcal{S}(Z, z)$, redshift, and resolution.

Additionally, the analytical fit fails to match the low-metallicity $\mathcal{S}(Z, z)$ in a complex way, variable depending on the TNG resolution modeled. For TNG100-1 and TNG300-1, the fit underestimates the high- z , low- Z tail of the metallicity distribution by up to an order of magnitude. For TNG50-1, the fit overestimates $\mathcal{S}(Z, z)$ by about a factor of 2. This can affect the modeling of populations at high redshifts and low metallicities ($Z/Z_{\odot} \lesssim 10^{-2}$). When using the analytical fit to model $\mathcal{S}(Z, z)$, the high mass rate ($M_1 \gtrsim 20 M_{\odot}$) is increasingly suppressed with increasing primary mass at $z_{\text{merger}} = 0.2$. This includes the flattening of the peaks near $33 M_{\odot}$ and $45 M_{\odot}$. As we do not model binaries with $Z < 10^{-4}$ ($Z/Z_{\odot} < 7 \times 10^{-3}$), these effects are less prominent in our BBH populations than those from the high metallicity $\mathcal{S}(Z, z)$ fit.

The cosmological simulation resolution primarily impacts the normalization of $\mathcal{S}(Z, z)$ and the resulting BBH population properties, though the analytical model for TNG50-1 (high resolution) most accurately represents the shape of its $\mathcal{S}(Z, z)$. At lower resolution (TNG300-1), the rates are lower and the disagreement between analytical fit and the simulation $\mathcal{S}(Z, z)$ is greatest. We will explore this dependence in more detail in future work.

As upcoming observing runs and next-generation gravitational-wave detectors are expected to detect stellar-mass BBH mergers to increasingly larger redshifts, the comparison of the observed population with models produced using different star formation history assumptions may be able to provide greater constraints on realistic star formation histories based on the redshift evolution of population properties. However, we emphasize the need to be cautious when using simple analytical fits to represent more complex underlying data, such as those from cosmological simulations. As analytical models smooth over features that cannot be captured

with their limited number of parameters, we may lose valuable information regarding the underlying physics and impact further analyses that are based upon those simplified models.

6. ACKNOWLEDGMENTS

E.B. and S.L. are supported by NSF Grants No. AST-2307146, No. PHY-2513337, No. PHY-090003, and No. PHY-20043, by NASA Grant No. 21-ATP21-0010, by John Templeton Foundation Grant No. 62840, by the Simons Foundation [MPS-SIP-00001698, E.B.], by the Simons Foundation International [SFI-MPS-BH-00012593-02], and by Italian Ministry of Foreign Affairs and International Cooperation Grant No. PGR01167. S.L. was additionally supported by the William H. Miller III Graduate Fellowship. L.v.S. acknowledges support from the Dutch Research Council (NWO) through the NWO Talent Programme (Veni, Grant DOI: <https://doi.org/10.61686/XVIAV86753>).

This work was carried out at the Advanced Research Computing at Hopkins (ARCH) core facility (<https://www.arch.jhu.edu/>), which is supported by the NSF Grant No. OAC-1920103. A.R. acknowledges financial support from the European Research Council for the ERC Consolidator grant DEMOBLACK, under contract no. 770017 and from the German Excellence Strategy via the Heidelberg Cluster of Excellence (EXC 2181 - 390900948) STRUCTURES.

This work made use of the following software packages: `astropy` (Astropy Collaboration et al. 2013, 2018, 2022), `Jupyter` (F. Perez & B. E. Granger 2007; T. Kluyver et al. 2016), `matplotlib` (J. D. Hunter 2007), `numpy` (C. R. Harris et al. 2020), `python` (G. Van Rossum & F. L. Drake 2009), `scipy` (P. Virtanen et al. 2020; R. Gommers et al. 2022), `Cython` (S. Behnel et al. 2011), `h5py` (A. Collette 2013; A. Collette et al. 2023), and `seaborn` (M. L. Waskom 2021).

Simulations in this paper made use of the `COMPAS` rapid binary population synthesis code (version 02.26.03, which is freely available at <http://github.com/TeamCOMPAS/COMPAS> (J. Riley et al. 2022). Model of gravitational wave selection effects based on J. W. Barrett et al. (2018). The STROOPWAFEL adaptive importance sampling algorithm is from F. S. Broekgaarden et al. (2019). Integration over cosmic star formation history outlined in (C. J. Neijssel et al. 2019). COMPAS' model of (pulsational) pair instability supernova is from S. Stevenson et al. (2019). Pulsar spin and magnetic field evolution is from D. Chattopadhyay et al. (2020). Model of chemically homogeneous evolution is from J. Riley et al. (2021).

Software citation information aggregated using `The Software Citation Station` (T. Wagg & F. S. Broekgaarden 2024; T. Wagg et al. 2025).

REFERENCES

Andrews, B. H., & Martini, P. 2013, *ApJ*, 765, 140, doi: [10.1088/0004-637X/765/2/140](https://doi.org/10.1088/0004-637X/765/2/140)

Artale, M. C., Mapelli, M., Bouffanais, Y., et al. 2020, *MNRAS*, 491, 3419, doi: [10.1093/mnras/stz3190](https://doi.org/10.1093/mnras/stz3190)

Artale, M. C., Mapelli, M., Giacobbo, N., et al. 2019, *MNRAS*, 487, 1675, doi: [10.1093/mnras/stz1382](https://doi.org/10.1093/mnras/stz1382)

Asplund, M., Amarsi, A. M., & Grevesse, N. 2021, *A&A*, 653, A141, doi: [10.1051/0004-6361/202140445](https://doi.org/10.1051/0004-6361/202140445)

Astropy Collaboration, Robitaille, T. P., Tollerud, E. J., et al. 2013, *A&A*, 558, A33, doi: [10.1051/0004-6361/201322068](https://doi.org/10.1051/0004-6361/201322068)

Astropy Collaboration, Price-Whelan, A. M., Sipőcz, B. M., et al. 2018, *AJ*, 156, 123, doi: [10.3847/1538-3881/aabc4f](https://doi.org/10.3847/1538-3881/aabc4f)

Astropy Collaboration, Price-Whelan, A. M., Lim, P. L., et al. 2022, *ApJ*, 935, 167, doi: [10.3847/1538-4357/ac7c74](https://doi.org/10.3847/1538-4357/ac7c74)

Barrett, J. W., Gaebel, S. M., Neijssel, C. J., et al. 2018, *MNRAS*, 477, 4685, doi: [10.1093/mnras/sty908](https://doi.org/10.1093/mnras/sty908)

Behnel, S., Bradshaw, R., Citro, C., et al. 2011, *Computing in Science Engineering*, 13, 31, doi: [10.1109/MCSE.2010.118](https://doi.org/10.1109/MCSE.2010.118)

Belczynski, K., Kalogera, V., & Bulik, T. 2002, *ApJ*, 572, 407, doi: [10.1086/340304](https://doi.org/10.1086/340304)

Belczynski, K., Kalogera, V., Rasio, F. A., et al. 2008, *ApJS*, 174, 223, doi: [10.1086/521026](https://doi.org/10.1086/521026)

Boco, L., Lapi, A., Chruścińska, M., et al. 2021, *ApJ*, 907, 110, doi: [10.3847/1538-4357/abd3a0](https://doi.org/10.3847/1538-4357/abd3a0)

Boesky, A. P., Broekgaarden, F. S., & Berger, E. 2024, *ApJ*, 976, 23, doi: [10.3847/1538-4357/ad7fe4](https://doi.org/10.3847/1538-4357/ad7fe4)

Boogaard, L. A., Brinchmann, J., Bouché, N., et al. 2018, *A&A*, 619, A27, doi: [10.1051/0004-6361/201833136](https://doi.org/10.1051/0004-6361/201833136)

Briel, M. M., Eldridge, J. J., Stanway, E. R., Stevance, H. F., & Chrimes, A. A. 2022, *MNRAS*, 514, 1315, doi: [10.1093/mnras/stac1100](https://doi.org/10.1093/mnras/stac1100)

Broekgaarden, F. S., Justham, S., de Mink, S. E., et al. 2019, *MNRAS*, 490, 5228, doi: [10.1093/mnras/stz2558](https://doi.org/10.1093/mnras/stz2558)

Broekgaarden, F. S., Berger, E., Neijssel, C. J., et al. 2021, *MNRAS*, 508, 5028, doi: [10.1093/mnras/stab2716](https://doi.org/10.1093/mnras/stab2716)

Broekgaarden, F. S., Berger, E., Stevenson, S., et al. 2022, *MNRAS*, 516, 5737, doi: [10.1093/mnras/stac1677](https://doi.org/10.1093/mnras/stac1677)

Chattopadhyay, D., Stevenson, S., Hurley, J. R., Rossi, L. J., & Flynn, C. 2020, MNRAS, 494, 1587, doi: [10.1093/mnras/staa756](https://doi.org/10.1093/mnras/staa756)

Chruścińska, M. 2024, Annalen der Physik, 536, 2200170, doi: [10.1002/andp.202200170](https://doi.org/10.1002/andp.202200170)

Chruścińska, M., Curti, M., Pakmor, R., et al. 2025, arXiv e-prints, arXiv:2511.15782, doi: [10.48550/arXiv.2511.15782](https://doi.org/10.48550/arXiv.2511.15782)

Chruścińska, M., & Nelemans, G. 2019, MNRAS, 488, 5300, doi: [10.1093/mnras/stz2057](https://doi.org/10.1093/mnras/stz2057)

Chruścińska, M., Nelemans, G., & Belczynski, K. 2019, MNRAS, 482, 5012, doi: [10.1093/mnras/sty3087](https://doi.org/10.1093/mnras/sty3087)

Collette, A. 2013, Python and HDF5 (O'Reilly)

Collette, A., Kluyver, T., Caswell, T. A., et al. 2023,, 3.8.0 Zenodo, doi: [10.5281/zenodo.7560547](https://doi.org/10.5281/zenodo.7560547)

Curti, M., Mannucci, F., Cresci, G., & Maiolino, R. 2020, MNRAS, 491, 944, doi: [10.1093/mnras/stz2910](https://doi.org/10.1093/mnras/stz2910)

Dominik, M., Belczynski, K., Fryer, C., et al. 2013, ApJ, 779, 72, doi: [10.1088/0004-637X/779/1/72](https://doi.org/10.1088/0004-637X/779/1/72)

Enia, A., Talia, M., Pozzi, F., et al. 2022, ApJ, 927, 204, doi: [10.3847/1538-4357/ac51ca](https://doi.org/10.3847/1538-4357/ac51ca)

Feldmann, R., Quataert, E., Faucher-Giguère, C.-A., et al. 2023, MNRAS, 522, 3831, doi: [10.1093/mnras/stad1205](https://doi.org/10.1093/mnras/stad1205)

Fishbach, M., & Kalogera, V. 2021, ApJL, 914, L30, doi: [10.3847/2041-8213/ac05c4](https://doi.org/10.3847/2041-8213/ac05c4)

Fishbach, M., & van Son, L. 2023, ApJL, 957, L31, doi: [10.3847/2041-8213/ad0560](https://doi.org/10.3847/2041-8213/ad0560)

Furlong, M., Bower, R. G., Theuns, T., et al. 2015, MNRAS, 450, 4486, doi: [10.1093/mnras/stv852](https://doi.org/10.1093/mnras/stv852)

Gao, F., & Han, L. 2012, Comput. Optim. Appl., 51, 259, doi: [10.1007/s10589-010-9329-3](https://doi.org/10.1007/s10589-010-9329-3)

Giacobbo, N., Mapelli, M., & Spera, M. 2018, MNRAS, 474, 2959, doi: [10.1093/mnras/stx2933](https://doi.org/10.1093/mnras/stx2933)

Gommers, R., Virtanen, P., Burovski, E., et al. 2022,, v1.8.1 Zenodo, doi: [10.5281/zenodo.6560517](https://doi.org/10.5281/zenodo.6560517)

Harris, C. R., Millman, K. J., van der Walt, S. J., et al. 2020, Nature, 585, 357, doi: [10.1038/s41586-020-2649-2](https://doi.org/10.1038/s41586-020-2649-2)

Hendriks, D. D., van Son, L. A. C., Renzo, M., Izzard, R. G., & Farmer, R. 2023, MNRAS, 526, 4130, doi: [10.1093/mnras/stad2857](https://doi.org/10.1093/mnras/stad2857)

Hopkins, P. F., Wetzel, A., Wheeler, C., et al. 2023, MNRAS, 519, 3154, doi: [10.1093/mnras/stac3489](https://doi.org/10.1093/mnras/stac3489)

Hunter, J. D. 2007, Computing in Science & Engineering, 9, 90, doi: [10.1109/MCSE.2007.55](https://doi.org/10.1109/MCSE.2007.55)

Hurley, J. R., Pols, O. R., & Tout, C. A. 2000, MNRAS, 315, 543, doi: [10.1046/j.1365-8711.2000.03426.x](https://doi.org/10.1046/j.1365-8711.2000.03426.x)

Hurley, J. R., Tout, C. A., & Pols, O. R. 2002, MNRAS, 329, 897, doi: [10.1046/j.1365-8711.2002.05038.x](https://doi.org/10.1046/j.1365-8711.2002.05038.x)

Hwang, H. S., Shin, J., & Song, H. 2019, MNRAS, 489, 339, doi: [10.1093/mnras/stz2136](https://doi.org/10.1093/mnras/stz2136)

Iacobelli, F., Mancarella, M., Foffa, S., & Maggiore, M. 2022, ApJ, 941, 208, doi: [10.3847/1538-4357/ac9cd4](https://doi.org/10.3847/1538-4357/ac9cd4)

Katsianis, A., Yang, X., & Zheng, X. 2021, ApJ, 919, 88, doi: [10.3847/1538-4357/ac11f2](https://doi.org/10.3847/1538-4357/ac11f2)

Katsianis, A., Gonzalez, V., Barrientos, D., et al. 2020, MNRAS, 492, 5592, doi: [10.1093/mnras/staa157](https://doi.org/10.1093/mnras/staa157)

Kennicutt, Jr., R. C. 1989, ApJ, 344, 685, doi: [10.1086/167834](https://doi.org/10.1086/167834)

Kluyver, T., Ragan-Kelley, B., Pérez, F., et al. 2016, in Positioning and Power in Academic Publishing: Players, Agents and Agendas, ed. F. Loizides & B. Schmidt, IOS Press, 87 – 90

Kroupa, P. 2001, MNRAS, 322, 231, doi: [10.1046/j.1365-8711.2001.04022.x](https://doi.org/10.1046/j.1365-8711.2001.04022.x)

Langer, N., & Norman, C. A. 2006, ApJL, 638, L63, doi: [10.1086/500363](https://doi.org/10.1086/500363)

Levina, S. 2026,, v1.0 Zenodo, doi: [10.5281/zenodo.18384088](https://doi.org/10.5281/zenodo.18384088)

Ma, X., Hopkins, P. F., Faucher-Giguère, C.-A., et al. 2016, MNRAS, 456, 2140, doi: [10.1093/mnras/stv2659](https://doi.org/10.1093/mnras/stv2659)

Madau, P., & Dickinson, M. 2014, ARA&A, 52, 415, doi: [10.1146/annurev-astro-081811-125615](https://doi.org/10.1146/annurev-astro-081811-125615)

Madau, P., & Fragos, T. 2017, ApJ, 840, 39, doi: [10.3847/1538-4357/aa6af9](https://doi.org/10.3847/1538-4357/aa6af9)

Magnelli, B., Adscheid, S., Wang, T.-M., et al. 2024, A&A, 688, A55, doi: [10.1051/0004-6361/202450081](https://doi.org/10.1051/0004-6361/202450081)

Mandel, I., & Broekgaarden, F. S. 2022, Living Reviews in Relativity, 25, 1, doi: [10.1007/s41114-021-00034-3](https://doi.org/10.1007/s41114-021-00034-3)

Mandel, I., & Farmer, A. 2022, PhR, 955, 1, doi: [10.1016/j.physrep.2022.01.003](https://doi.org/10.1016/j.physrep.2022.01.003)

Mannucci, F., Salvaterra, R., & Campisi, M. A. 2011, MNRAS, 414, 1263, doi: [10.1111/j.1365-2966.2011.18459.x](https://doi.org/10.1111/j.1365-2966.2011.18459.x)

Mapelli, M., & Giacobbo, N. 2018, MNRAS, 479, 4391, doi: [10.1093/mnras/sty1613](https://doi.org/10.1093/mnras/sty1613)

Mapelli, M., Giacobbo, N., Ripamonti, E., & Spera, M. 2017, MNRAS, 472, 2422, doi: [10.1093/mnras/stx2123](https://doi.org/10.1093/mnras/stx2123)

Mapelli, M., Giacobbo, N., Santoliquido, F., & Artale, M. C. 2019, MNRAS, 487, 2, doi: [10.1093/mnras/stz1150](https://doi.org/10.1093/mnras/stz1150)

Marchant, P., Pappas, K. M. W., Gallegos-Garcia, M., et al. 2021, A&A, 650, A107, doi: [10.1051/0004-6361/202039992](https://doi.org/10.1051/0004-6361/202039992)

Marinacci, F., Baldi, M., Iorio, G., et al. 2025, arXiv e-prints, arXiv:2510.06311.

<https://arxiv.org/abs/2510.06311>

Marinacci, F., Pakmor, R., & Springel, V. 2014, MNRAS, 437, 1750, doi: [10.1093/mnras/stt2003](https://doi.org/10.1093/mnras/stt2003)

Marinacci, F., Vogelsberger, M., Pakmor, R., et al. 2018, MNRAS, 480, 5113, doi: [10.1093/mnras/sty2206](https://doi.org/10.1093/mnras/sty2206)

Naiman, J. P., Pillepich, A., Springel, V., et al. 2018, MNRAS, 477, 1206, doi: [10.1093/mnras/sty618](https://doi.org/10.1093/mnras/sty618)

Neijssel, C. J., Vigna-Gómez, A., Stevenson, S., et al. 2019, MNRAS, 490, 3740, doi: [10.1093/mnras/stz2840](https://doi.org/10.1093/mnras/stz2840)

Nelson, D., Pillepich, A., Springel, V., et al. 2018, MNRAS, 475, 624, doi: [10.1093/mnras/stx3040](https://doi.org/10.1093/mnras/stx3040)

Nelson, D., Springel, V., Pillepich, A., et al. 2019a, Computational Astrophysics and Cosmology, 6, 2, doi: [10.1186/s40668-019-0028-x](https://doi.org/10.1186/s40668-019-0028-x)

Nelson, D., Pillepich, A., Springel, V., et al. 2019b, MNRAS, 490, 3234, doi: [10.1093/mnras/stz2306](https://doi.org/10.1093/mnras/stz2306)

Nocedal, J., & Wright, S. 2006, Numerical optimization, 2nd edn., Springer series in operations research and financial engineering (New York, NY: Springer). http://gso.gbv.de/DB=2.1/CMD?ACT=SRCHA&SRT=YOP&IKT=1016&TRM=ppn+502988711&sourceid=fbw_bibsonomy

Olejak, A., Belczynski, K., & Ivanova, N. 2021, A&A, 651, A100, doi: [10.1051/0004-6361/202140520](https://doi.org/10.1051/0004-6361/202140520)

Pakmor, R., Simpson, C. M., van de Voort, F., et al. 2022, MNRAS, 512, 3602, doi: [10.1093/mnras/stac717](https://doi.org/10.1093/mnras/stac717)

Panter, B., Heavens, A. F., & Jimenez, R. 2004, MNRAS, 355, 764, doi: [10.1111/j.1365-2966.2004.08355.x](https://doi.org/10.1111/j.1365-2966.2004.08355.x)

Perez, F., & Granger, B. E. 2007, Computing in Science and Engineering, 9, 21, doi: [10.1109/MCSE.2007.53](https://doi.org/10.1109/MCSE.2007.53)

Pillepich, A., Springel, V., Nelson, D., et al. 2018a, MNRAS, 473, 4077, doi: [10.1093/mnras/stx2656](https://doi.org/10.1093/mnras/stx2656)

Pillepich, A., Nelson, D., Hernquist, L., et al. 2018b, MNRAS, 475, 648, doi: [10.1093/mnras/stx3112](https://doi.org/10.1093/mnras/stx3112)

Pillepich, A., Nelson, D., Springel, V., et al. 2019, MNRAS, 490, 3196, doi: [10.1093/mnras/stz2338](https://doi.org/10.1093/mnras/stz2338)

Planck Collaboration. 2016, A&A, 594, A13, doi: [10.1051/0004-6361/201525830](https://doi.org/10.1051/0004-6361/201525830)

Planck Collaboration. 2020, A&A, 641, A6, doi: [10.1051/0004-6361/201833910](https://doi.org/10.1051/0004-6361/201833910)

Popesso, P., Concas, A., Cresci, G., et al. 2023, MNRAS, 519, 1526, doi: [10.1093/mnras/stac3214](https://doi.org/10.1093/mnras/stac3214)

Riley, J., & Mandel, I. 2023, ApJ, 950, 80, doi: [10.3847/1538-4357/accf90](https://doi.org/10.3847/1538-4357/accf90)

Riley, J., Mandel, I., Marchant, P., et al. 2021, MNRAS, 505, 663, doi: [10.1093/mnras/stab1291](https://doi.org/10.1093/mnras/stab1291)

Riley, J., Agrawal, P., Barrett, J. W., et al. 2022, ApJS, 258, 34, doi: [10.3847/1538-4365/ac416c](https://doi.org/10.3847/1538-4365/ac416c)

Rocha, K. A., Hur, R., Kalogera, V., et al. 2025, ApJ, 983, 39, doi: [10.3847/1538-4357/adb970](https://doi.org/10.3847/1538-4357/adb970)

Romagnolo, A., Belczynski, K., Klencki, J., et al. 2023, MNRAS, 525, 706, doi: [10.1093/mnras/stad2366](https://doi.org/10.1093/mnras/stad2366)

Romagnolo, A., Klencki, J., Vigna-Gómez, A., & Belczynski, K. 2025, A&A, 693, A137, doi: [10.1051/0004-6361/202452169](https://doi.org/10.1051/0004-6361/202452169)

Romero-Shaw, I., Hirai, R., Bahramian, A., Willcox, R., & Mandel, I. 2023, MNRAS, 524, 245, doi: [10.1093/mnras/stad1732](https://doi.org/10.1093/mnras/stad1732)

Roy, S. K., van Son, L. A. C., Ray, A., & Farr, W. M. 2025, ApJL, 985, L33, doi: [10.3847/2041-8213/add34a](https://doi.org/10.3847/2041-8213/add34a)

Santoliquido, F., Mapelli, M., Artale, M. C., & Boco, L. 2022, MNRAS, 516, 3297, doi: [10.1093/mnras/stac2384](https://doi.org/10.1093/mnras/stac2384)

Santoliquido, F., Mapelli, M., Bouffanais, Y., et al. 2020, ApJ, 898, 152, doi: [10.3847/1538-4357/ab9b78](https://doi.org/10.3847/1538-4357/ab9b78)

Santoliquido, F., Mapelli, M., Giacobbo, N., Bouffanais, Y., & Artale, M. C. 2021, MNRAS, 502, 4877, doi: [10.1093/mnras/stab280](https://doi.org/10.1093/mnras/stab280)

Savaglio, S., Glazebrook, K., Le Borgne, D., et al. 2005, ApJ, 635, 260, doi: [10.1086/497331](https://doi.org/10.1086/497331)

Schaye, J., Crain, R. A., Bower, R. G., et al. 2015, MNRAS, 446, 521, doi: [10.1093/mnras/stu2058](https://doi.org/10.1093/mnras/stu2058)

Schiebelbein-Zwack, A., & Fishbach, M. 2024, ApJ, 970, 128, doi: [10.3847/1538-4357/ad5353](https://doi.org/10.3847/1538-4357/ad5353)

Schmidt, M. 1959, ApJ, 129, 243, doi: [10.1086/146614](https://doi.org/10.1086/146614)

Sgalletta, C., Mapelli, M., Boco, L., et al. 2024, arXiv e-prints, arXiv:2410.21401, doi: [10.48550/arXiv.2410.21401](https://doi.org/10.48550/arXiv.2410.21401)

Smith, T., & Kaplinghat, M. 2024, in American Astronomical Society Meeting Abstracts, Vol. 243, American Astronomical Society Meeting Abstracts, 206.17

Speagle, J. S., Steinhardt, C. L., Capak, P. L., & Silverman, J. D. 2014, ApJS, 214, 15, doi: [10.1088/0067-0049/214/2/15](https://doi.org/10.1088/0067-0049/214/2/15)

Spera, M., & Mapelli, M. 2017, MNRAS, 470, 4739, doi: [10.1093/mnras/stx1576](https://doi.org/10.1093/mnras/stx1576)

Spera, M., Mapelli, M., Giacobbo, N., et al. 2019, MNRAS, 485, 889, doi: [10.1093/mnras/stz359](https://doi.org/10.1093/mnras/stz359)

Springel, V. 2010, MNRAS, 401, 791, doi: [10.1111/j.1365-2966.2009.15715.x](https://doi.org/10.1111/j.1365-2966.2009.15715.x)

Springel, V., White, S. D. M., Jenkins, A., et al. 2005, Nature, 435, 629, doi: [10.1038/nature03597](https://doi.org/10.1038/nature03597)

Stevenson, S., Sampson, M., Powell, J., et al. 2019, ApJ, 882, 121, doi: [10.3847/1538-4357/ab3981](https://doi.org/10.3847/1538-4357/ab3981)

Tang, P. N., Eldridge, J. J., Stanway, E. R., & Bray, J. C. 2020, MNRAS, 493, L6, doi: [10.1093/mnrasl/slz183](https://doi.org/10.1093/mnrasl/slz183)

The LIGO Scientific Collaboration, the Virgo Collaboration, the KAGRA Collaboration, et al. 2025, arXiv e-prints, arXiv:2508.18083, doi: [10.48550/arXiv.2508.18083](https://doi.org/10.48550/arXiv.2508.18083)

Turbang, K., Lalleman, M., Callister, T. A., & van Remortel, N. 2024, ApJ, 967, 142, doi: [10.3847/1538-4357/ad3d5c](https://doi.org/10.3847/1538-4357/ad3d5c)

Van Rossum, G., & Drake, F. L. 2009, Python 3 Reference Manual (Scotts Valley, CA: CreateSpace)

van Son, L. 2023, <https://zenodo.org/records/7612755>

van Son, L. A. C., de Mink, S. E., Chruścińska, M., et al. 2023, *ApJ*, 948, 105, doi: [10.3847/1538-4357/acbf51](https://doi.org/10.3847/1538-4357/acbf51)

van Son, L. A. C., de Mink, S. E., Renzo, M., et al. 2022a, *ApJ*, 940, 184, doi: [10.3847/1538-4357/ac9b0a](https://doi.org/10.3847/1538-4357/ac9b0a)

van Son, L. A. C., de Mink, S. E., Callister, T., et al. 2022b, *ApJ*, 931, 17, doi: [10.3847/1538-4357/ac64a3](https://doi.org/10.3847/1538-4357/ac64a3)

van Son, L. A. C., Roy, S. K., Mandel, I., et al. 2025, *ApJ*, 979, 209, doi: [10.3847/1538-4357/ada14a](https://doi.org/10.3847/1538-4357/ada14a)

Vargas-Salazar, I., Oey, M. S., Eldridge, J. J., et al. 2025, arXiv e-prints, arXiv:2506.13004, doi: [10.48550/arXiv.2506.13004](https://doi.org/10.48550/arXiv.2506.13004)

Virtanen, P., Gommers, R., Oliphant, T. E., et al. 2020, *Nature Methods*, 17, 261, doi: [10.1038/s41592-019-0686-2](https://doi.org/10.1038/s41592-019-0686-2)

Vogelsberger, M., Marinacci, F., Torrey, P., & Puchwein, E. 2020, *Nature Reviews Physics*, 2, 42, doi: [10.1038/s42254-019-0127-2](https://doi.org/10.1038/s42254-019-0127-2)

Vogelsberger, M., Genel, S., Springel, V., et al. 2014, *MNRAS*, 444, 1518, doi: [10.1093/mnras/stu1536](https://doi.org/10.1093/mnras/stu1536)

Wagg, T., Broekgaarden, F., Van-Lane, P., Wu, K., & Gültekin, K. 2025,, v1.4 Zenodo, doi: [10.5281/zenodo.1765485](https://doi.org/10.5281/zenodo.1765485)

Wagg, T., & Broekgaarden, F. S. 2024, arXiv e-prints, arXiv:2406.04405. <https://arxiv.org/abs/2406.04405>

Waskom, M. L. 2021, *Journal of Open Source Software*, 6, 3021, doi: [10.21105/joss.03021](https://doi.org/10.21105/joss.03021)

Willcox, R., Schneider, F. R. N., Laplace, E., et al. 2025, arXiv e-prints, arXiv:2510.07573, doi: [10.48550/arXiv.2510.07573](https://doi.org/10.48550/arXiv.2510.07573)

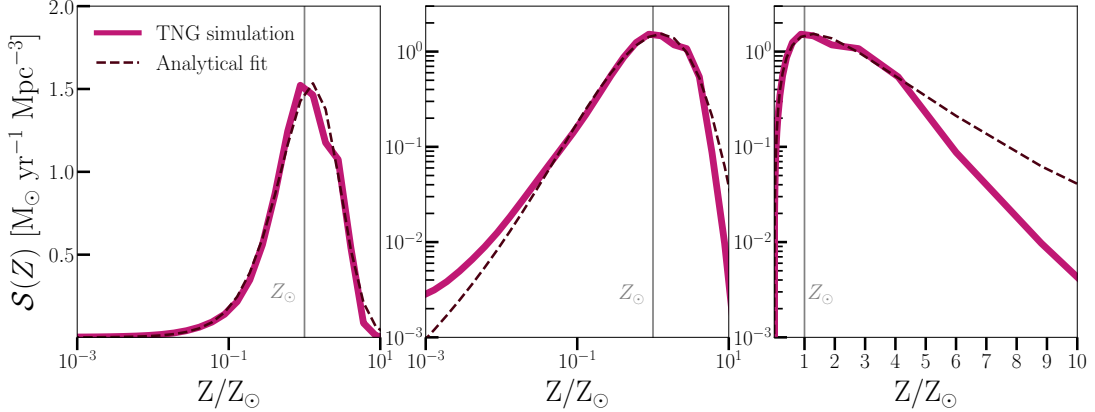


Figure 11. The metallicity distribution $\mathcal{S}(Z)$ for TNG100-1. The solid magenta line is the simulation-based $\mathcal{S}(Z)$ and the dashed line is the fit-based $\mathcal{S}(Z)$. Left: only the horizontal axis on a logarithmic scale; middle: both axes on a logarithmic scale; right: only vertical axis on a logarithmic scale. Note that the vertical axis limits differ between the left and the other two panels. The vertical gray line indicates solar metallicity, for reference.

APPENDIX

A. IMPACT OF AXIS SCALING ON INTERPRETATION OF THE FIT TO $\mathcal{S}(Z)$

In Section 3.1, $\mathcal{S}(Z)$ is shown using different axis scalings to visually connect Figure 2 and the right panel of Figure 3. In the former, both axes are logarithmic, whereas in the latter the metallicity distribution is shown on a linear vertical scale with logarithmic metallicity. These different representations lead to apparent differences in the shape of $\mathcal{S}(Z)$, which can obscure specific aspects of the fit depending on the metallicity range of interest. To clarify how the choice of axis scaling affects the interpretation of $\mathcal{S}(Z)$, Figure 11 presents the metallicity distribution using three different combinations of linear and logarithmic axes. When $\mathcal{S}(Z)$ is plotted linearly against $\log(Z/Z_\odot)$ (right panel, analogous to the right panel of Figure 3), the behavior of the fit near the peak of the metallicity distribution is emphasized. In contrast, using logarithmic scaling on both axes (middle panel, analogous to Figure 2) highlights deviations at low and high metallicities, where the values of $\mathcal{S}(Z, z)$ are small but important for merging BBH formation. Finally, plotting metallicity linearly while scaling $\mathcal{S}(Z)$ logarithmically (left panel) further emphasizes differences near the peak and at super-solar metallicities. We note that COMPAS does not model binaries with metallicities above $Z > 0.03$, corresponding to $Z/Z_\odot \gtrsim 2.11$, which limits the interpretation of the distribution at the highest metallicities.

B. DIFFERENCE BETWEEN FIT-BASED AND SIMULATION-BASED MASS DISTRIBUTIONS

To identify which binary systems are misrepresented by the analytical $\mathcal{S}(Z, z)$ fit, we examine the mass distribution of the excess BBH mergers that are over-predicted by the analytical $\mathcal{S}(Z, z)$ relative to the TNG simulation $\mathcal{S}(Z, z)$. Figure 12 highlights the redshift dependence of the excess structure near $M_{\text{BH},1} \simeq 8 M_\odot$ that arises in the mass distribution when the fit is used. This behavior explains the apparent disappearance of the $\sim 8 M_\odot$ feature at $z \gtrsim 2$ in the total mass distributions (Figure 6), while demonstrating that a residual excess persists at $\sim 8 M_\odot$ across all redshifts, alongside a secondary excess near the peak $M_{\text{BH},1} \simeq 16 M_\odot$ at $z \gtrsim 2$.

At low redshift ($z \lesssim 2$), the difference between the fit and simulation mass distributions peaks near $M_{\text{BH},1} \simeq 8 M_\odot$. As redshift increases, the dominant peak shifts toward higher primary masses, reaching $\sim 16 M_\odot$, while a smaller bump near $8 M_\odot$ remains. For TNG50-1, the overproduction at $z_{\text{merger}} = 0.2$ reaches $\sim 4 \text{ Gpc}^{-3} \text{ yr}^{-1} M_\odot^{-1}$ near $8 M_\odot$, increasing to approximately $\sim 6 \text{ Gpc}^{-3} \text{ yr}^{-1} M_\odot^{-1}$ at $z_{\text{merger}} = 2$. At higher redshifts, the peak difference decreases and levels off to $\sim 3 \text{ Gpc}^{-3} \text{ yr}^{-1} M_\odot^{-1}$. At higher primary masses ($M_{\text{BH},1} \gtrsim 16 M_\odot$), the analytical fit instead underpredicts the merger rate by up to 1–2 $\text{Gpc}^{-3} \text{ yr}^{-1} M_\odot^{-1}$, with the largest discrepancy occurring around $z_{\text{merger}} = 1$.

Finally, the magnitude of the excess shows a clear dependence on resolution. At $M_{\text{BH},1} \simeq 8 M_\odot$, the difference between the fit-based and simulation-based mass distributions in TNG50-1 is approximately a factor of two larger than in TNG-100-1, and $\sim 3 - 4$ times larger than in TNG300-1. This trend indicates that resolution-dependent

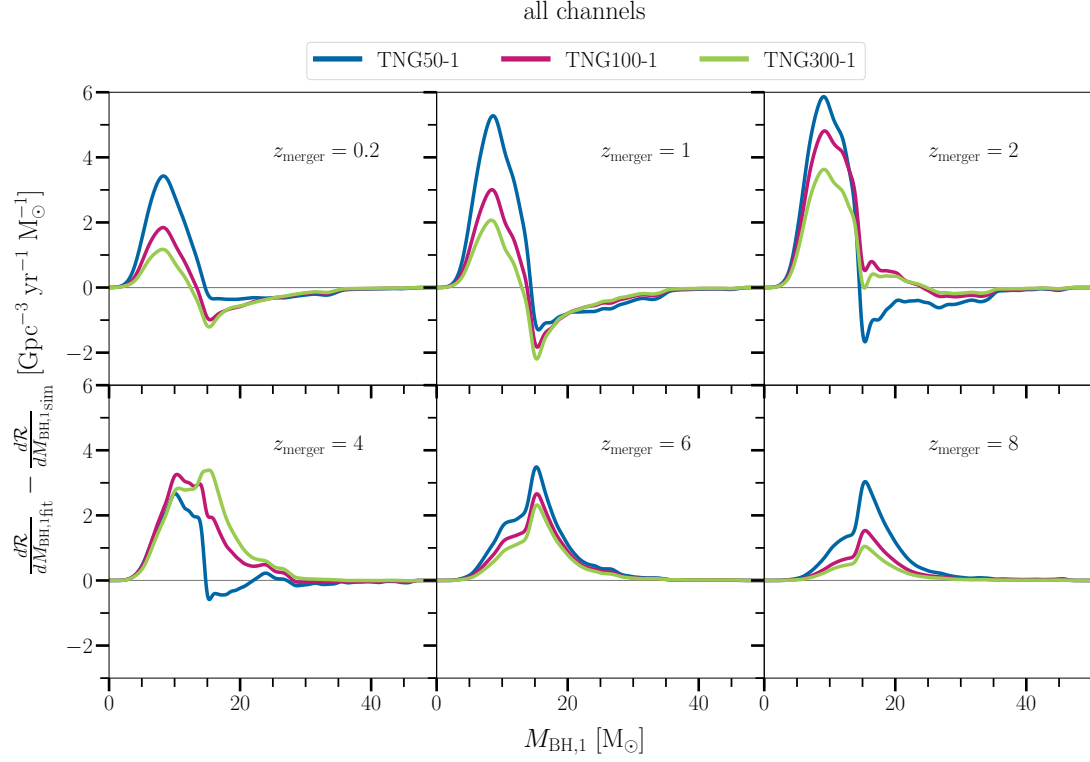


Figure 12. Difference between the BBH primary-mass distributions obtained using the analytical fit $\mathcal{S}(Z, z)$ and the TNG simulation $\mathcal{S}(Z, z)$, shown for $z_{\text{merger}} = 0.2, 1, 2, 4, 6, 8$.

features in the simulated $\mathcal{S}(Z, z)$ directly propagate into the predicted BBH mass distributions when using analytical fits.